Imaging of 3-dimensional Structure of the Subduction Zone, Central New Zealand

by

Xun Luo Jim Ansell

Institute of Geophysics,
Research School of Earth Sciences,
Victoria University of Wellington,
Wellington, New Zealand

June 1994.

A research report prepared for
The Earthquake Commission.
(Research Grant Number: 93/118)

ABSTRACT

A 3-dimensional P-velocity structure of the subduction zone under central New Zealand is imaged using 32,512 first P-arrivals and 8,025 S-arrivals from 3,340 earthquakes occurred in this region since 1986 and using a seismic tomographic method. Detailed structures in the overlying Australian plate and in the subducted Pacific plate are studied based on the obtained seismic tomographic results. The subduction interface is determined to vary in the direction parallel to the strike of the subducted plate and to be broken under northern Cook Strait. On the southern North Island, the Pacific plate not only is subducted northwest, but also dips down towards northeast at a shallow dipping angle. This northeast dipping structure is found to be the main reason for the high apparent Pn velocities which have been observed in the Cape Palliser region. The shallowest subduction interface is determined to be at the depth of approximately 13 km under Cape Palliser. From a 3-dimensional finite-difference flexural analysis on a significant change in depth of the interface, a torn structure in the subducted crust is found to be located under northern Cook Strait and to be approximately perpendicular to the strike of subduction. This torn structure is shown to be extended downwards to as deep as 40 km. It is presumed to be the largest fault trending NW-SE under central New Zealand. The subduction interface is shown to have very different shape on each side of the torn structure. On the southern side the subduction plate is found to be approximately 7-10 km deeper than that on the northern side. Under the top of the South Island the interface appears to have a southwest down-dipping curvature. Evidence from seismic images shows that the Wairau Fault extends northeast to the North Island along the east coast of the Marlborough Sounds and between the offshore of the west coast and the east of Kapiti Island towards onshore at the northwest of Otaki. An offset or bent structure of this fault is shown near the western offshore of the Wellington Peninsula where the torn structure is found. The velocity structure suggests that the northern extension of the Wairau Fault extend downward to at least 20 km. It is presumed to be another major fault and geological boundary trending NE-SW in central New Zealand. A narrow high velocity zone is obtained above the subducted interface, along the east coast near Cape Palliser and presumed to be the reason of a horst-like subduction structure or the intrusion of fast volcanic rocks in the bottom of the overlying plate. Offshore of east Cape Palliser, a low velocity region is found. The Australian crust under Cook Strait is characterized by nearly square regions of both high and low velocity perturbations. An extensive faulting system dominated by faults in NE-SW and NW-SE trends is suggested in the Cook Strait crust.

CONTENTS

1. INTRODUCTION

1.1 Geological and tectonic setting

The central region of New Zealand which includes the southern North Island, the Cook Strait and the northern South Island, lies at the frontal margin of the Australian plate (Fig. 1). The Pacific plate is being subducted obliquely northwest beneath the Australian plate and dips towards a depth of at least 250km (Adams and Ware 1977). To the east is the Hikurangi Trough which defines the beginning of the subduction of the Pacific plate and is obliquely terminated south of this region where an intra-continental transform system occurs (Lewis and Davey 1987). To the west exists a back-arc basin, the Wanganui Basin, which is considered to be a result of subduction thrusting (Stern et al. 1992a). The motion of the Pacific plate relative to the Australian plate varies from 50mm/yr at an angle of $60-80^{\circ}$ to the margin in the northeast of the region to 40mm/yr, almost transcurrent, in the south (Chase 1978, Walcott 1978a). The collision of the two plates creates extensive east-west compression in the crust of the overlying plate and causes several major right-lateral strike-slip faults in this central region (Bibby 1976, Walcott 1978b, Reyners 1980, Robinson 1986).

The central region can be roughly divided into several subregions on the basis of on-surface geological structures and geophysical characteristics. The Wairarapa fault, one of the major right-lateral faults in the southern North Island, separates the southern North Island into two geological subregions. The western side is extensively underlain by uplift Triassic greywacke where another major fault, the Wellington fault, is well developed. Tertiary sediments and greywacke basement of Jurassic age overlies the east side of the Wairarapa fault. These two subregions show a strong contrast in seismic velocities (Robinson 1986). The Wairau fault in the northern South Island, which is considered to be the extension of the Alpine Fault (Bibby 1976), exists as a boundary of the western Late Paleozoic schists and eastern Jurassic greywacke. All of the major faults in both North Island and South Island are terminated at the Cook Strait. Their extensions are of a matter of some debate. Although a continuation of these faults across Cook Strait has been suggested (Lensen 1958; Suggate 1963; Stevens 1974; Carter et al. 1988) strong evidence for continuation has not yet been established.

1.2 Seismicity

Central New Zealand is one of the most active earthquake zones in this country. An intensive earthquake belt of approximate 250km in width stretches northeast and parallels the Hikurangi Margin (Adams and Ware 1977; Hatherton 1980; Reyners 1989; Anderson and Webb 1994).

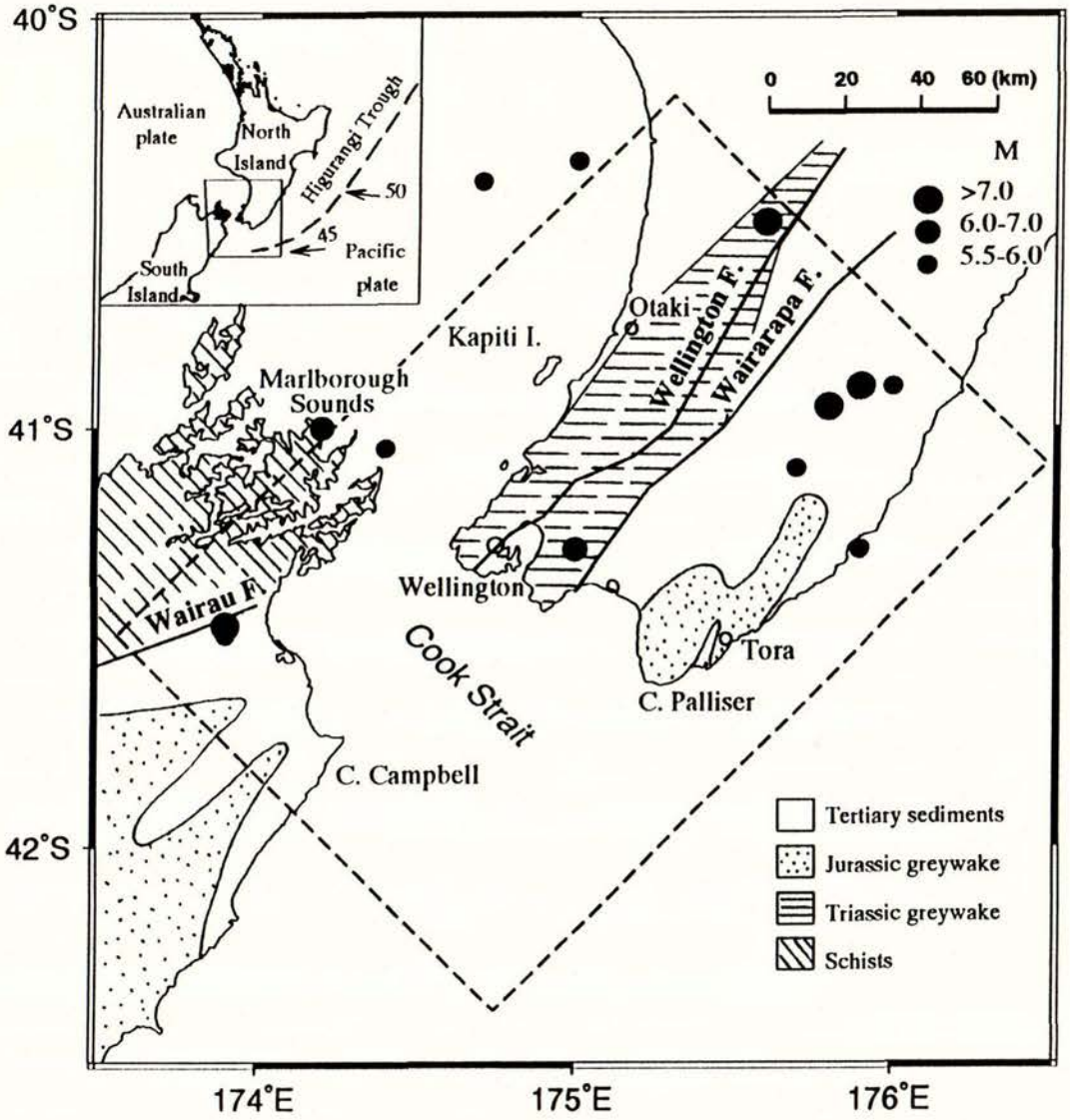

Fig. 1 Map of central New Zealand, showing geological structures (generalized from Suggate and Grindley 1972) and historical damaging earthquakes (filled circles; from Eiby 1968, 1980), where M denotes earthquake magnitude. The oblique dashed rectangular represents the region in which a 3-dimensional subduction structure is studied in this work. *Insert:* the tectonic setting of the North Island; the square represents the position of this map. The relative motion data (in mm/yr) are from Walcott (1978a).

A band of seismicity defined within a thickness of approximately 40km and delineating the area of active subduction in this region, extends northwest from about 14km deep under the east coast, down to a depth of at least 250km under the west of the region (Robinson 1986; Reyners 1989; Luo 1992; Anderson and Webb 1994). A study of historical seismicity has shown that quite a few large earthquakes have occurred in the central New Zealand since 1460 (Eiby 1968). The largest earthquake of 1855 (approximately M=8.0) which was believed to occur somewhere in the Wellington region was probably the most severe earthquake in this country since that time. It was accompanied by a large offset on the Wairarapa fault (Ongley 1943) with up to 3m vertical and 12m right-lateral displacements, and affected an area of at least 12,000 km^2 (Robinson 1986). Other large historical earthquakes with determined locations, including the 1948 Wairau earthquake (M=7.1) (Eiby 1980), the Pahiatua earthquake (M=7.1) of 1934, the Masterton earthquakes (M=7.0 and 7.1) are shown in Fig. 1. In the central region, there has been a relatively quiet period for very large earthquakes (M>7) since 1942. This may be at least partly attributable to the state of the subduction interface which is found to be locked at this stage (Walcott 1978b, Robinson 1986). Elastic strain is accumulating in this region and the potential for very large earthquakes on this interface appears to exist (Robinson 1986, Ansell and Bannister 1991, Galea 1992). The recurrence time of these large earthquakes in the Wellington region has been roughly estimated at 100-150 yr (Stevens 1974, Walcott 1978b).

1.3 Previous studies of the subduction structure

The earliest broad structure of the region was determined by Bullen (1939, 1955) using regional earthquake phases. Later, the velocity structure was refined using the results of a large seismic refraction experiment, along a line extending 177 km northeast from Wellington (Garrick 1968). The crustal-mantle interface appeared to exist at a depth of about 36 km and was assumed to be horizontal. A layer , from about 23 to 36 km above the Moho, was inferred as comprising the crustal part of the Pacific plate. Extensive earthquake studies across central North Island have identified the subduction structure in this region. The Pacific crust has been found to be subducted northwest from 14km down to at least 250km under central New Zealand (Adams and Ware 1977, Reyners 1980, Robinson 1986, Luo 1992). The dipping angle of the subducted plate was determined to be approximately 5^{o} at the east coast (Reyners 1980, Davey et al. 1986), increase below the central region and reache a steep angle of about $60 - 70^{o}$ to the west of the region (Adams and Ware 1977, Reyners 1989, Anderson and Webb 1994). A seismic reflection experiment, along a line perpendicular to the earlier refraction experiment and across the Wellington city, revealed a relatively detailed crustal structure (Davey and Smith 1983). The plate interface was identified as dipping north-west from a depth of 18km below the Wairarapa fault and 33 km under the

Wellington region. A segmented subduction plate under this region was first proposed by Reyners (1983), based on the distribution of seismicity and stresses in the subducted plate. He speculated that a torn structure in the Pacific plate exists somewhere beneath Cook Strait. The segmentation was further studied by Robinson (1986), who has found that the subducted plate is 5-10km deeper south of Cook Strait.

Seismic velocities have been found to vary greatly in the overlying Australian plate (Robinson 1983, 1986; Luo 1992). Robinson (1986) derived velocity distributions for regions inside the Wellington Seismic Network. Significant east-west velocity variation in the overlying crust was found, with 18% for P-wave and 12% for S-wave, decreasing to the east. The upper mantle velocity, Pn, has been found to be regionally distributed (Haines 1979, Kayal 1983), with a value of 8.5 km/s dominating the region. Very high apparent P-wave velocities, 7.8, 8.9 and 9.0 km/s have been observed in the Wellington region (Kayal and Smith 1984, Galea 1992, Reyners 1991). These velocities have been found to be anomalously larger than known upper mantle P-velocities and this is difficult to interpret. Previous seismic experiments and inversions were carried out using two dimensional configurations. A 3-dimensional tomographic method is used in this study in order to obtained the details of the subduction interface and the general subduction structure in this region. These results will improve our critical understanding of geological and the seismic processes in this vulnerable region of New Zealand.

1.4 The study region

The subduction structure to be studied is constrained within a rectangular region with horizontal dimensions 140 x 205 km, where the 4 conners have the following latitudes and longitudes $(-41.50^{\circ}, 173.56^{\circ})$, $(-42.38^{\circ}, 174.75^{\circ})$, $(-41.09^{\circ}, 176.48^{\circ})$, $(-40.19^{\circ}, 175.30^{\circ})$, and depth range of 0-80 km (Fig. 1). This study region contains a part of the subduction zone comprising the overlying Australian plate and the north-west subducted Pacific plate. This region is oriented at 45° northeast, in order to make two of the coordinates x and y which specify the study region lie approximately perpendicular to the dipping subduction plate and parallel to the trend of the Hikurangi Trough, respectively.

2. METHOD

2.1 Travel-time residual system

The objective of 3-dimensional seismic tomography is to image the subsurface velocity

structures in terms of the travel-time residuals of P- and S-waves. In general, the relationship between the observed arrival time from source i to station j and the seismic velocity distribution through which the ray travels is

$$T_{ij}^{obs} = \int_{L_{ij}} \frac{1}{V(\mathbf{x})} dl + t_{i0} = \int_{L_{ij}} S(\mathbf{x}) dl + t_{i0} \tag{1}$$

where i=1,2,...,n; j=1,,2,...,m; $\mathbf{x} = (x_1, x_2, x_3)$ represents 3-dimensional coordinates; $V(\mathbf{x})$ is a 3-dimensional velocity distribution; L_{ij} is the ray-path from source i to station j; t_{i0} denotes the origin time of the source and $S(\mathbf{x})$ is slowness, the inverse of velocity $V(\mathbf{x})$; dl is the differential of path length.

The ray-path of a seismic wave depends upon the unknown velocity structure which is to be determined. This causes the seismic travel-time to be related nonlinearly to the velocity structure. A common approach to processing equation (1) is to linearize using the Fermat's Principle: the travel-time is stationary along the actual ray-path. In other word, the small perturbations along the ray-path produce a second-order error in the travel-time. Here, the slowness $S(\mathbf{x})$ is substituted by an initial model $S_0(\mathbf{x})$ and a slowness perturbation $\delta S(\mathbf{x})$.

Thus, equation (1) is written as

$$t_{ij}^{obs} = T_{ij}^{obs} - t_{i0} = \int_{L_{ij}(S_0(\mathbf{x})+\delta S(\mathbf{x}))} [S_0(\mathbf{x}) + \delta S(\mathbf{x})] dl$$

$$= \int_{L_{ij}(S_0(\mathbf{x}))} [S_0(\mathbf{x}) + \delta S(\mathbf{x})] dl + O(\delta S^2(\mathbf{x})) \tag{2}$$

where $O(\delta S^2(\mathbf{x}))$ are the high order perturbations.

Then, the real ray-path is approximately represented by the ray-path determined in the initial model. This linearization simplifies the inversion problem and enables us to use standard linear inverse theory. Neglecting the higher order perturbation term and rearranging (2), we obtain a travel-time residual equation

$$\delta T_{ij} = t_{ij}^{obs} - t_{ij}^{cal} = \int_{L_{ij}(S_0(\mathbf{x}))} \delta S dl \tag{3}$$

where:

$$t_{ij}^{cal} = \int_{L_{ij}(S_0(\mathbf{x}))} S_0(\mathbf{x}) dl \tag{4}$$

is the calculated travel-time obtained on the initial model. The travel-time residual, in principle, represents the difference between the observed and calculated travel-times which is caused by the difference between the true and the initial models. The objective is now to obtained the model difference using a large set of travel-time residuals.

In practice, the foci of earthquakes are always located approximately on a reference model beforehand. The calculated travel-times t_{ij}^{cal} are always obtained from ray tracing starting at these mislocated sources. Therefore, the travel-time residual of equation (3) contains not only information of the perturbations of the initial velocity model, but also the mislocations. In addition, the station term at each of the stations (receivers) needs also to be accounted for in the travel-time residual equation. These station terms include the the part of the observed travel-time residuals induced by the small scale geological structure near the station which can not be resolved by model parametrization, the errors in the observed travel-times resulting from instrument errors and systematic phase mispicks. Therefore, introducing the mislocation corrections and station terms into eq. (3) prevents the part of the residuals produced by these factors to be incorrectly explained by velocity perturbations.

Thus, we need to solve the velocity and earthquake location perturbations as well as the station term simultaneously. The physical situation is modeled by the mathematical expression

$$\delta T_{ij} = \int_{L_{ij}(S_0(\mathbf{x}))} \delta S(\mathbf{x}) dl + \frac{\partial t_{ij}}{\partial x_1} \delta x_{1i} + \frac{\partial t_{ij}}{\partial x_2} \delta x_{2i} + \frac{\partial t_{ij}}{\partial x_3} \delta x_{3i} + \delta t_i + \delta t_j \tag{5}$$

where t_{ij} is the travel-time of the ray (i, j); δx_{1i}, δx_{2i}, δx_{3i}, δt_i are the perturbations of the three position coordinates and origin-time of earthquake i and δt_j is the station term of station j.

The integral of the slowness perturbation in eq. (5) can be approximated in a discrete expression when the velocity model is parameterized in either a grid or a block configuration. If a grid model parameterization is used, the integral term can be approximated as a summation of segments (Luo 1994)

$$\int_{L_{ij}(S_0(\mathbf{x}))} \delta S(\mathbf{x}) = \sum_{p=1}^{np} b_{ijp} \delta V_p \tag{6}$$

where np is the total number of model grid points; δV_p is the velocity perturbation at grid point p and b_{ijp} is the interpolation coefficient at p (see Luo 1994). When all of the observations are considered, this system can be expressed in matrix notation as follows

$$\delta \mathbf{T} = (\mathbf{B}\ \mathbf{H}\ \mathbf{G})\,(\delta \mathbf{V}\ \ \delta \mathbf{h}\ \ \delta \mathbf{g})^T \tag{7}$$

where $\delta \mathbf{T}$ denotes the vector of travel-time residuals; **B**, **H** and **G** are the matrices of interpolation coefficients (corresponding to velocity perturbations), partial derivatives of earthquake locations and partial derivatives of station terms, respectively; $\delta \mathbf{V}$, $\delta \mathbf{h}$ and $\delta \mathbf{g}$ are vectors of velocity perturbations, perturbations to the hypocenters and station terms, respectively; T denotes the matrix transpose.

In eq. (7) the vector of the travel-time residuals $\delta \mathbf{T}$ and the coefficients in **B, H, G** can be obtained once an initial model is specified. In this study the calculations of the travel-time (4) and the coefficients were completed using a 3-dimensional ray-tracing method developed by Luo (1994), based on the Complete Ray-Tracing procedure of Červený et al. (1988).

Solving eq. (7) directly involves the assumption that all the observed data have equal significance. However, the data used are usually contaminated by observational errors with different levels. In order to prevent the inversion result to be overwhelmed by poor quality data, a down-weighting to the data with relatively larger errors can be performed before inversion. The estimation of the weighting values are based normally on the uncertainties or standard errors of travel-time residuals (Crosson 1976, Pulliam et al. 1993, Rowan and Clayton 1993). The weighting is actually applied to each row of the residual system, equivalent to applying a diagonal weighting matrix to eq. (7) by left multiplication.

Additionally, owing to the different scales of the coefficients in the coefficient matrix which correspond to different physical properties (velocity, hypocentre and station term) a direct inversion of eq. (7) may also produce deleterious effects on the inversion results (Nolet 1987, Pulliam et al. 1993). The unknowns corresponding to larger coefficient values will be over-weighted in the inversion. In addition, since rays are not uniformly distributed in a study region, the unknowns must be sampled in different number of times. The unknowns which are heavily sampled by seismic rays will also be over-weighted in the inversion. In order to obtain reasonable inversion results, rescaling should be applied to the coefficients to change their values to appropriate amplitudes. As the rescaling deals with individual unknowns, the rescaling values are applied to each of the columns of the matrix. This is done by right-multiplying the coefficient matrix using a diagonal matrix with specified rescaling values.

Therefore, the final travel-time residual system is as follows

$$\delta\tilde{\mathbf{T}} = \tilde{\mathbf{A}}\delta\tilde{\mathbf{x}} \tag{8}$$

where $\delta\tilde{\mathbf{T}} = \mathbf{W}_t\delta\mathbf{T}$, $\mathbf{W}_t$ is the diagonal weighting matrix; $\tilde{\mathbf{A}} = \mathbf{W}_t(\mathbf{B}\ \mathbf{H}\ \mathbf{G})\mathbf{R}_x$, $\mathbf{R}_x$ is the diagonal rescaling matrix; and $\delta\mathbf{x} = \mathbf{R}_x\delta\tilde{\mathbf{x}} = (\delta\mathbf{V}\ \ \delta\mathbf{h}\ \ \delta\mathbf{g})^T$.

2.2 Inversion method

Recently, with more and more high quality seismic data becoming available the number of observations used for seismic tomography has increased greatly. The large number of data sets allows the velocity model to be much more finely parameterized, producing a very large number of unknowns (velocities at grid points and earthquake locations) to be obtained. Hence, the size of the coefficient matrix becomes very large and sparse. Finding a solution from such a travel-time system using direct inversion methods such as *singular value decomposition* (Lawson and Hanson 1974; Aki et al. 1977) and the *damping least squares method* (Aki et al. 1977), which involve the transformation of large matrices, becomes impossible owing to the restrictions of computer storage and computation time. Therefore, another approach which is able to solve the problem of storage and which has acceptable computation efficiency must be used. Such an approach is invariably iterative. Recently, the seismic tomographic inversion has been performed extensively using iterative algorithms (Clayton and Comer 1984; Spakman and Nolet 1988; Zhao and Hasegawa 1993; and many others). All of these iterative techniques are the so-called 'row action methods'. They process the equations of the system one by one. At each iterative step, the old solution is over-written by the newly obtained solution. The iteration continues step by step until certain convergence criteria are satisfied. Using iterative methods, only the nonzero coefficients are processed. It is not necessary to store the coefficient matrix which contains a large percentage zeros. As the computation of the iterative inversion only applies to nonzero coefficients so that the computation is fast.

In this study, the LSQR algorithm of Paige and Saunders (1982a,b) was used. This method incorporates Lanczos' iteration (Lanczos 1950) into a conjugate gradient (CG) method and produces least-squares solutions similar to *singular value decomposition* (Spakman and Nolet 1988). Theoretically, LSQR will converge to the true least-squares solution in n iterations, where n is the number of unknowns. In practice, the procedure is stopped after a certain number of iterations as n is always very large in seismic tomographic applications. The limited number of iterations becomes one of the advantages for LSQR in seismic tomography as seismic tomographic

problems are always ill-conditioned. The LSQR method starts the construction of the solution by neglecting those components corresponding the smallest singular values of the coefficient matrix. As the iterations proceed, the smallest singular values interfere more with the solution (Paige and Saunders 1982a,b). Therefore, the relatively few iterations can prevent the strong affection of the smallest singular values on the inversion results so as to obtained more reasonable solutions. Both numerical and practical experiments have shown that LSQR displays much faster convergence behavior and produces more acceptable results when it is used on singular and ill-conditioned problems than any of the other iterative methods (Nolet 1985; van der Sluis and van der Vorst 1987; Spakman and Nolet 1988; Vasco 1991; Pulliam et al. 1993). Because of these advantages, LSQR has been widely used in seismic tomographic inversion. It is also the preferred choice in the inversions of this study.

3. SEISMIC NETWORK AND DATA SET

3.1 Seismic stations

Earthquakes occurring in the study region are monitored by the permanent stations of the Wellington Seismograph Network (WSN) and the National Standard Network (NSN), which cover the southern North Island and the top of the South Island (Fig. 2). WSN has been equipped with a digital SNARE recording system (Gledhill and Randall 1986) since September 1986. The seismic signals of one (Z, vertical) or three components (Z, N-S and E-W) from seismometers with a natural period of 1.0 second are digitized at a sampling rate of 50 Hz and are recorded on magnetic tape at the central site. The timing error among its stations is considered to be within ± 0.02 s (Webb, pers. comm. 1993). 17 seismic stations of WSN from different periods of operation were used in this study. Only 3 stations from NSN are located in the study region which were equipped also with digital recording seismographs. Seismic signals were recorded independently on tape at each of the NSN station sites. Timing error among these stations is considered to be less than ± 0.05 s (Webb, pers. comm. 1993). In order to increase the coverage of seismic stations to improve velocity inversion quality, stations of several temporary seismic arrays were used to supplement the permanent station data base. These temporary networks and arrays comprise the Wellington Regional Array (WRA), Porirua Array (PRA), Lower Hutt Array (LHA), Kapiti Array (KTA), Leeds University Array (LUA), Hikurangi Seismic Array (HSA) and VUW Array at Cape Palliser (VUW). The portable 3-component digital EARSS seismographs (Gledhill 1991a) were deployed for the stations of WRA (Gledhill 1991b), PRA and LHA (Taber and Smith 1992), KTA (Taber and Richardson 1992), HSA (Reyners 1991) and VUW (Luo 1992), using seismometers

with a natural period of 1.0 second. The sampling rate of 100 Hz was used for these seismographs except those of HSA which used 200 Hz sampling rate. It is considered that the timing accuracy among the EARSS seismographs in an array lies within ±0.02 s. 7 RATS seismographs were also used in the WRA survey (Gledhill 1991c). The RATS seismograph only monitors the vertical component of ground motion and therefore only the first arrivals of P-phase were used. The RATS seismograph used a similar method to EARSS to maintain timing accuracy (Gledhill 1991c). The Leeds University Array (LUA) consisted of 9 Guralp broad-band 3-component digital seismographs running at a sampling interval of 50 Hz. The records selected from this array are with a timing accuracy within ±0.02 s. 64 seismic stations in total were used in this study, comprising the best station coverage ever obtained for this region. The locations of the stations are displyed in Fig. 2 and their details are listed in Table 1.

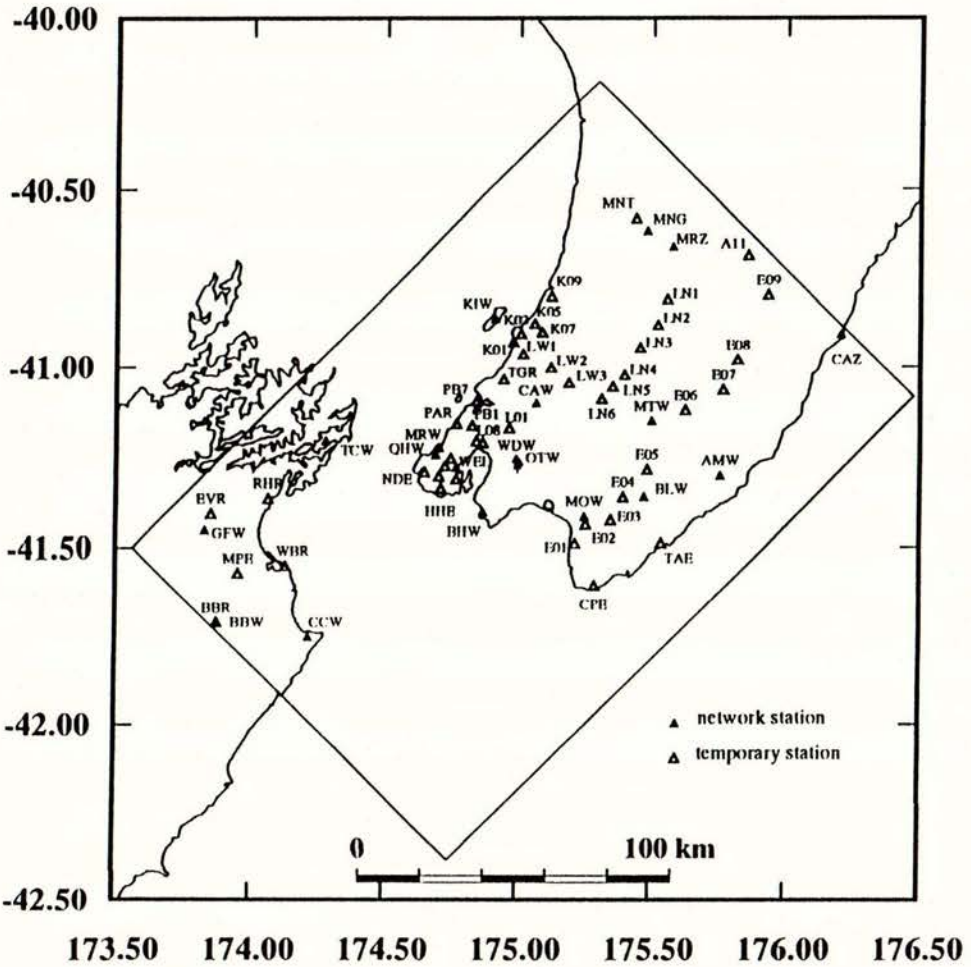

Fig. 2 64 seismic stations from permanent and temporary seismic networks used in this study.

Table 1 Locations and period of operation of the seismic stations of the Wellington Network (WSN), National Network (NSN), the Wellington Regional Array (WRA), the Porirua Array (PRA), the Lower Hutt Array (LHA), the Kapiti Array (KTA), the Leeds University Array (LUA), the Hikurangi Seismic Array (HSA), the Victoria University Array (VUW). and two temporary stations. Their positions are plotted in Fig. 2.

Stn	ZNE	Latitude	Longitude	Altitude	period of operation	Note
AMW	Z	-41.3094	175.7608	0.29	23/03/91-07/12/92	WSN stn
BBW	Z	-41.7125	173.8783	0.25	01/06/92-28/02/93	..
BHW	Z	-41.4092	174.8714	0.01	08/01/87-27/02/93	..
BLW	Z	-41.3686	175.4747	0.34	01/10/86-28/02/93	..
CAW	Z	-41.1088	175.0678	0.33	01/10/86-28/02/93	..
CCW	Z	-41.7547	174.2150	0.22	01/10/86-28/02/93	..
GFW	Z	-41.4567	173.8306	0.23	08/12/91-28/02/93	..
KIW	Z	-40.8638	174.9117	0.32	01/10/86-28/02/93	..
MOW	Z	-41.4217	175.2519	0.43	01/10/86-28/02/93	..
MRW	ZNE	-41.2325	174.7050	0.24	01/10/86-28/02/93	..
MTW	Z	-41.1594	175.5019	0.28	01/10/86-28/02/93	..
OTW	Z	-41.2775	175.0042	0.02	01/08/92-28/02/93	..
QHW	ZNE	-41.2519	174.6906	0.19	01/10/86-01/08/88	..
TCW	Z	-41.2133	174.2758	0.15	01/10/86-28/02/93	..
WDW	Z	-41.2686	174.9936	0.13	01/10/86-25/03/92	..
WEL	ZNE	-41.2861	174.7683	0.12	01/10/86-25/02/93	..
MNG	Z	-40.6186	175.4819	0.40	30/01/87-28/02/93	NSN stn
MRZ	Z	-40.6625	175.5792	0.32	08/04/92-28/02/93	..
CAZ	Z	-40.9042	176.2261	0.01	29/06/87-23/11/88	..
PB1	ZNE	-41.1722	174.8274	0.34	16/06/90-28/06/90	PRA stn
PB7	ZNE	-41.1033	174.8437	0.15	16/06/90-28/06/90	..
L01	ZNE	-41.1793	174.9671	0.05	29/11/90-16/12/90	LHA stn
L08	ZNE	-41.2190	174.8673	0.15	29/11/90-23/01/91	..
K01	ZNE	-40.9330	174.9798	0.01	28/01/92-21/02/92	KTA stn
K02	ZNE	-40.9086	175.0085	0.05	18/01/92-21/02/92	..
K05	ZNE	-40.8794	175.0595	0.04	10/01/92-23/02/92	..
K07	ZNE	-40.9041	175.0885	0.20	18/01/92-23/02/92	..
K09	ZNE	-40.8006	175.1223	0.04	22/01/92-23/02/92	..

Stn denotes station; ZNE denote the components of the seismograph, where Z is the vertical component, N is the north-south component and E is the east-west component. Altitude is in km.

Table 1 *(continued)*

Stn	ZNE	Latitude	Longitude	Altitude	period of operation	Note
BSE	ZNE	-41.3187	174.7691	0.10	31/01/89-03/07/89	WRA stn
HHE	ZNE	-41.3436	174.7112	0.46	11/02/89-01/07/89	..
KSE	ZNE	-41.3107	174.7043	0.09	31/01/89-03/07/89	..
MPE	ZNE	-41.5751	173.9539	0.12	22/03/89-29/05/89	..
NDE	ZNE	-41.2996	174.6496	0.38	22/03/89-03/07/89	..
PDD	ZNE	-41.2832	174.7263	0.19	31/01/89-03/07/89	..
PRE	ZNE	-41.2620	174.7478	0.23	04/02/89-20/06/89	..
BBR	Z	-41.7126	173.8756	0.30	01/04/89-29/05/89	..
EVR	Z	-41.4129	173.8534	0.10	03/04/89-20/05/89	..
HOR	Z	-41.2147	174.8431	0.28	06/04/89-31/05/89	..
PAR	Z	-41.1672	174.7688	0.16	07/04/89-31/05/89	..
RHR	Z	-41.3717	174.0627	0.18	02/04/89-28/05/89	..
TGR	Z	-41.0403	174.9453	0.22	06/04/89-31/05/89	..
WBR	Z	-41.5546	174.1286	0.02	01/04/89-24/05/89	..
LTN1	ZNE	-40.8094	175.5587	0.36	10/01/92-18/04/92	LUA stn
LTN2	ZNE	-40.8835	175.5232	0.28	10/01/92-18/04/92	..
LTN3	ZNE	-40.9492	175.4567	0.28	10/01/92-18/04/92	..
LTN4	ZNE	-41.0282	175.3991	0.15	10/01/92-18/04/92	..
LTN5	ZNE	-41.0614	175.3551	0.14	10/01/92-18/04/92	..
LTN6	ZNE	-41.0970	175.3144	0.13	10/01/92-18/04/92	..
LTW3	ZNE	-41.0505	175.1910	0.21	13/01/92-18/04/92	..
LTW2	ZNE	-41.0068	175.1229	0.21	10/01/92-18/04/92	..
LTW1	ZNE	-40.9674	175.0170	0.20	10/01/92-11/04/92	..
E01	ZNE	-41.4931	175.2175	0.02	17/04/91-19/04/91	HSA stn
E02	ZNE	-41.4424	175.2574	0.39	17/04/91-23/04/91	..
E03	ZNE	-41.4310	175.3511	0.40	17/04/91-23/04/91	..
E04	ZNE	-41.3685	175.3958	0.37	18/04/91-20/04/91	..
E05	ZNE	-41.2936	175.4857	0.11	17/04/91-20/04/91	..
E06	ZNE	-41.1289	175.6301	0.16	17/04/91-20/04/91	..
E07	ZNE	-41.0700	175.7717	0.24	17/04/91-22/04/91	..
E08	ZNE	-41.9836	175.8231	0.16	17/04/91-21/04/91	..
E09	ZNE	-41.7975	175.9328	0.37	17/04/91-22/04/91	..
CPE	ZNE	-41.6132	175.2915	0.01	05/10/90-07/10/90	VUW stn
TAE	ZN	-41.4927	175.5408	0.10	05/10/90-07/10/90	..
A11	Z	-40.6864	175.8594	0.15	07/02/93-19/02/93	Temp stn
MNT	Z	-40.5850	175.4394	0.39	31/07/91-28/11/91	..

3.2 Earthquake data set

Earthquakes are well distributed in this region in both the Pacific Plate and the Australian Plate. These earthquakes are located using the first P arrivals and S arrivals, recorded at the WSN and NSN stations (Anderson and Webb 1994) on a 1-dimensional reference velocity model (Lowry 1991). In this study, only earthquakes which have occurred since 1986 were used, when the digital seismic network WSN was founded. In order to use sufficient numbers of reliable recordings, only earthquakes of magnitude greater than 2.0 (M_L) were used. From a research of Luo (1994), earthquakes from a cluster of aftershocks will not improve the tomographic inversion results but do increase the computing burden of ray tracing. Therefore, these aftershocks were considered to be redundant and excluded from the earthquake data set. In addition, earthquakes which were located under the assumption of restricted depth (Anderson and Webb 1994) were also excluded from the data set because their estimated depths are not reliable. The selection of earthquakes was made according to the following requirements:

1) Earthquakes are required to be located within this research region (Fig. 1) and with depths no greater than 80 km.

2) Earthquakes with magnitudes less than 2.0 were rejected as they normally do not produce enough reliable arrival times.

3) Earthquakes should be evenly distributed. Most cluster aftershocks were considered to be redundant and were discarded.

4) Earthquakes which were located under the assumption of restricted depth were discarded as their estimated depths are not reliable.

5) Arrival times with quality factors larger than 1 for P-phase and larger than 3 for S-phase were rejected (see following).

6) Arrival times with travel-time residuals greater than 2 s for P-phase and 3.5 s for S-phase, obtained on the initial model, were discarded.

7) Each earthquake must have at least 8 arrival times.

3,340 earthquakes were finally selected. Their location accuracy is considered to be within ±3 km in the central region and within ±5 km at the edge of WSN, using the reference model. The epicentres of these earthquakes are plotted in Fig. 3. The projection of the hypocentres onto a north-east vertical cross section A-A' is shown in Fig. 4. A large number of the earthquakes occurred at depths between 15-50 km and show a banded and curved earthquake distribution. These earthquake locations were obtained from the New Zealand Earthquake Catalog supplied by the Seismological Observatory of DSIR (Department of Scientific and Industrial Research).

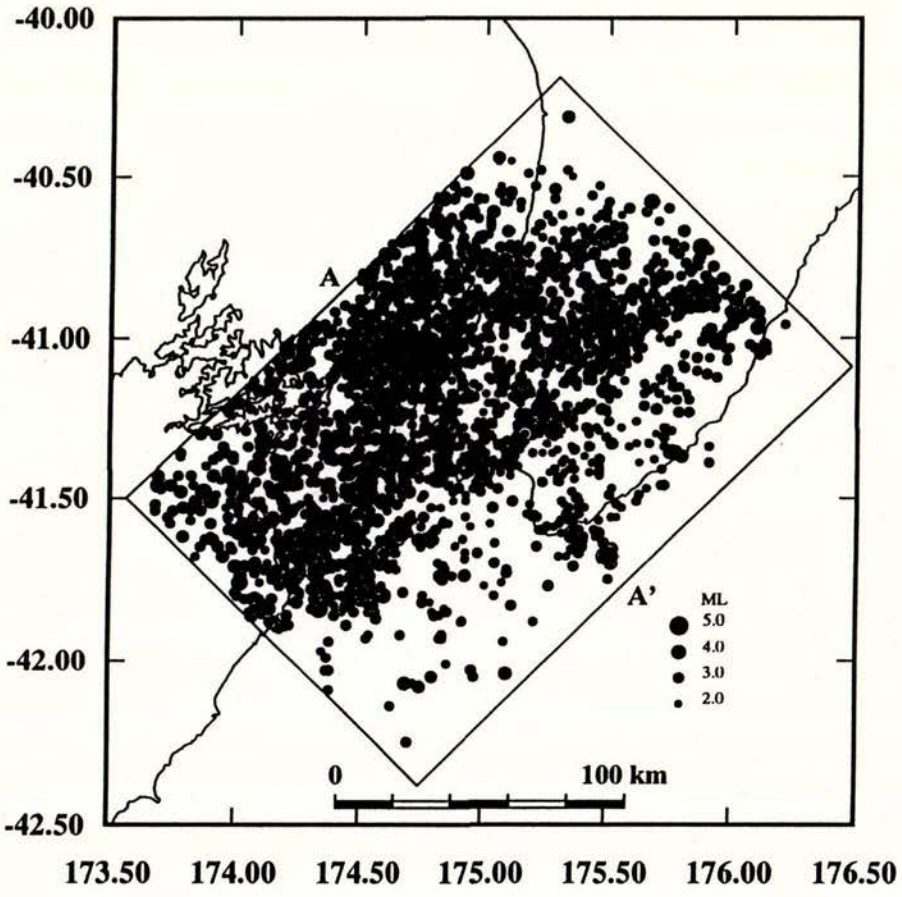

Fig. 3 The epicentres of the 3,340 earthquakes used in this study. A-A' denotes the cross section shown in Fig. 4.

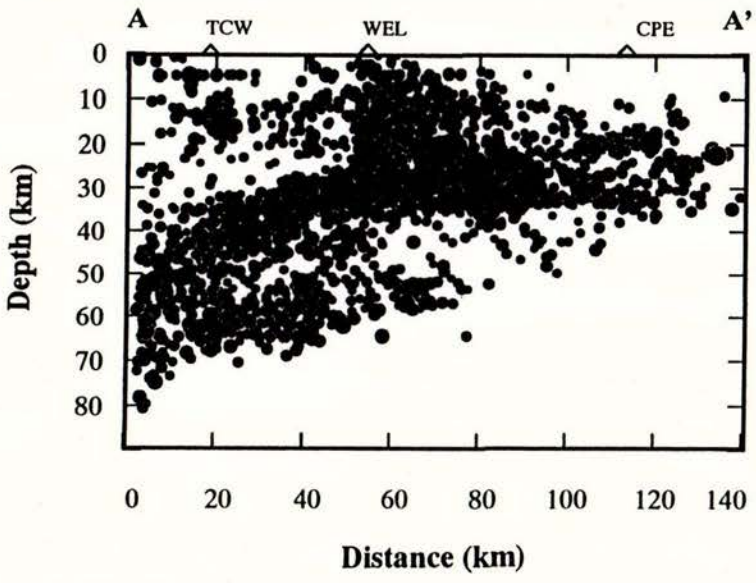

Fig. 4 The cross section A-A' of the projections of the 3,340 earthquakes and three seismic stations WEL, TCW and CPE.

3.3 P and S arrival times

The data set for seismic tomographic inversion is composed of the arrival times of the first P-phase as well as S-phase. Inclusion of S-phase has been found to improve greatly the constraint on the hypocentral parameters (Roecker 1982) so that more reliable inversion results for the velocity perturbations and the hypocentral parameters can be obtained. 80% of the arrival times used in this study came from arrivals recorded at the stations of the permanent Wellington Seismological Network (WSN) and National Network (NSN). These arrival times are listed in the New Zealand Earthquake Catalog. The uncertainties of P- and S-picks in the catalog are ranked in terms of quality factors ranging from 0 to 4, as shown in Table 2.

Table 2 Uncertainties of P- and S-phase picks defined by the Seismological Observatory of DSIR

Quality Factor	Accuracy, in seconds
0	$<\pm 0.10$
1	± 0.10 - ± 0.25
2	± 0.25 - ± 0.50
3	± 0.50 - ± 1.00
4	± 1.00 - ± 2.00

Most of the remaining 20% of the arrival times were determined by the authors from seismograms recorded at the stations of the temporary arrays (the picks from the Wellington Regional Array (WRA) were supplied by Dr. Gledhill and Mr. Chadwick). These seismograms were displayed on screen and the arrival times were picked from enlarged seismic traces with 0.01 s picking accuracy. The seismic signals recorded by the LUA broad-band seismographs were stacked on a long period (approximately 3 seconds) noise background. Most of the arrival times were determined directly from enlarged seismograms on screen without filtering. For the cases in which stacked signals were clipped off from screen or where the direct picking was considered to be inaccurate, filtering was applied to remove the noise background. In order to check the discrepancy between the travel-times picked by the authors and those listed in the earthquake catalog, seismic waveforms of several earthquakes which were randomly selected from the 3,340 earthquakes were redisplayed on screen and their first P and S arrival-times were determined. These arrival times were then compared with the published results. It was found that the

differences between these two results lie within ±0.07 s. The picks made by the authors were also ranked in terms of same quality factors as those of the catalog.

The 3,340 earthquakes produced 32,512 first arrivals for P- and 8,025 arrivals for S-phase, comprising 40,537 arrival times in total. The maximum number of stations which recorded any earthquake was 38. The arrival times with quality factors 0 and 1 comprise 90.6% of the whole data set. The details of the arrival times used in this study are listed in Table 3.

Table 3 Number of P and S picks used in this study

Phases	Quality Factor	Number of Picks	Percentage
P, S	0	24,424	60.2
P, S	1	12,307	30.4
S	2	2,836	7.0
S	3	970	2.4

In this study, only P velocity structures were obtained using both P and S arrival times at a velocity ratio (V_p/V_s) of 1.73. The S velocity structure was not studied because the coverage of S rays was very poor. In the following, the term "velocity" refers only to P-wave velocity.

4. NUMERICAL INVERSION AND RESULTS

4.1 Model parameterization

The 3-dimensional velocity model which was defined in a 140×205×80 km region was parameterized in terms of grid points, spaced 10 km apart on each of nine rectangular planes at depths of 5, 12, 20, 30, 40, 50, 60, 70 and 80 km below sea level (Fig. 5), comprising 2,223 grid points at each of which a seismic velocity perturbation was to be obtained.

As the study region is small, the Cartesian coordinate system was used and no correction for the ellipticity of the Earth (Dziewonski and Gilbert 1976) was applied to the arrival times. The origin of the Cartesian coordinate system was placed at the center of the plane (latitude –41.30°, longitude 175.00°) at the depth of 0 km, and is denoted by the symbol '+' beneath station OTW in Fig. 2. The x-axis was constrained to lie at 45° towards the southeast; the y-axis was in the direction 45° towards the northeast and the z-axis was specified upwards. The ground surface

was constructed using meshed ground elevation points and B-spline interpolation (Luo 1994). All of the seismic stations were put back to their true positions with elevation errors less than ±100 meters. No elevation correction was performed to any of the stations.

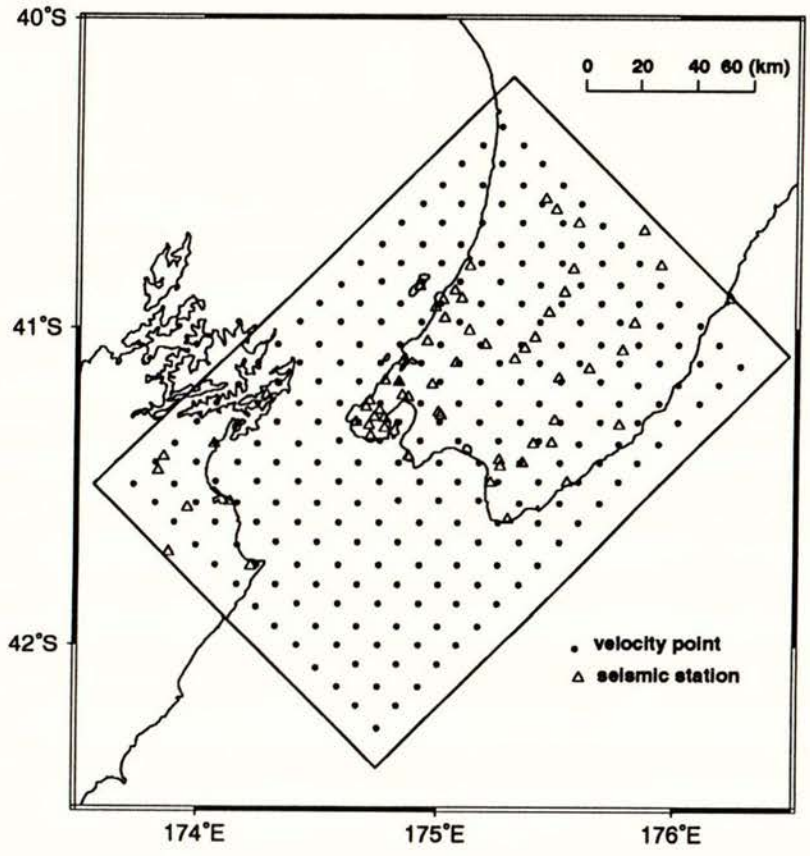

Fig. 5 Model parameterization for the seismic tomographic inversion. The velocity model is parameterized in terms of grid points (filled circles), spacing 10 km apart on each of nine rectangular planes located at depths of 5, 12, 20, 30, 40, 50, 60, 70 and 80 km below sea level.

Two velocity models were used in this study; a model with a continuous velocity distribution (Model A) and a model with a velocity discontinuity (Model B). Both models had the same parameterization but different initial velocities. In Model B a velocity discontinuity was assumed in order to simulate the subduction interface between the Australian plate and the Pacific plate.

4.2 Initial velocity structure of Model A

Using a suitable initial model is very important in seismic tomographic inversion. In order to obtain reliable results, the initial velocity structure should be chosen to be in agreement with the trend of the true velocity distribution (Luo 1994). Previous 2-dimensional seismic experiments have revealed a layered velocity structure with velocity increasing downwards (Garrick 1968; Davey and Smith 1983; Robinson 1986). From these results, an initial model with downward increasing velocity structure was considered to be the first-order approximation to the true velocity distribution and thus was used in this study. This velocity structure was assumed to vary continuously throughout the study region. The initial velocities at the nine depths were specified in reference to the velocity values of the 1-dimensional Wellington Model (Lowry 1991) on which the earthquake hypocenters used in this study were located. These initial velocity values are listed in Table 4 and this will be referred to as Model A.

Table 4 Initial velocities of Model A

Depth (km)	Velocity (km/s)
5	5.6
12	6.0
20	6.5
30	6.8
40	7.8
50	8.6
60	8.8
70	8.8
80	8.8

4.3 Forward ray tracing and inversion scheme

The travel-time residual system (eq. 8) was set up using the ray tracing technique developed by Luo (1994). Each of the 40,537 rays corresponding to P- and S-waves was traced individually from its origin (earthquake) to the corresponding target (station). The error limit of 200 m between a target location and a ray end point was used. In addition, the number of the initial velocities used for interpolating a velocity at a given point along a ray was 2 along each of the three coordinates (x, y and z). The forward ray tracing produced 40,537 travel-time residuals and the coefficients corresponding to the 2223 velocity perturbations, 13,360 location perturbations for the 3,340 earthquakes and 67 station terms. The total number of unknowns to be obtained was

15,650. The size of the coefficient matrix reached $40,537 \times 15,650$, in which 98% of the elements were zero, making this a very large and sparse matrix. The LSQR method (Paige and Saunders 1982) was used to solve this system.

4.4 Hitcounts

The coefficient corresponding to the velocity unknown at each grid point was calculated through velocity interpolation in forward ray tracing. If a ray travels through the vicinity of a grid point, its velocity is used in the interpolation. This point has then hit once and the coefficient corresponding to the velocity unknown of this point is calculated. One grid point may be hit many times by different rays. Therefore, the hitcount of a velocity grid point represents the sampling rate of this unknown made by seismic rays or equivalently the number of equations which contain the coefficient related to this velocity unknown. The hitcount is a useful parameter for assessing the quality of ray sampling for each velocity unknown. In general, the greater the sampling rate, the better the quality of the inversion result which can be obtained. Fig. 6 displays the hitcounts obtained at the grid points (unknowns) at the nine depths of Model A. The greater hitcounts are concentrated in the central regions at the shallow depths of 5 and 12 km. With increasing depth, the region of greater hitcounts shifts to the northwest in approximately agreement with the hypocentre distribution. The maximum sampling rate occurs at a point close to Wellington city, with the largest hitcounts of value 12,939. The regions below 50 km and at the edges of each depth plane are relatively poorly sampled.

4.5 Resolution

After a linear inversion it is normally required to assess the reliability of the obtained velocity solution. The conventional approaches for this assessment are carried out using the resolution and covariance matrices (Aki et al. 1977). However, at present these two assessment matrices cannot be obtained using any iterative algorithm. In this study, an alternative approach known as the 'checkerboard test' (Inoue et al. 1990) was used to assess the resolution of the LSQR iterative solution. Using the checkerboard test, the resolution assessment can be carried out either before real data inversion or after. In this study, the checkerboard test was carried out before the inversion in order to derive preliminary but important knowledge about the possible results from real data inversion.

In order to perform the checkerboard test, a synthetic positive (+0.3 km/s) or negative (-0.3 km/s) velocity perturbation was assigned alternately to each of the velocity solution elements (corresponding to each grid point). The synthetic travel-time system was calculated using both

the obtained coefficient matrix and the synthetic perturbations. In principle, if the coefficient matrix is not singular or ill-conditioned, the original synthetic perturbations will be fully recovered through an inversion of the synthetic system. Hence, the original 'checkerboard' can be completely reconstructed. If the matrix is singular or ill-conditioned, the system becomes underdetermined and some of the solutions will be smeared out. In this case, the full checkerboard cannot be recovered. The solutions with well defined positive and negative components which are consistent with the original distribution are considered to be well resolved. The smeared out solutions are poorly resolved.

In seismic tomography, the travel-time residual system is always ill-conditioned. In order to prevent the smallest singular values becoming involved in the inversion, the LSQR procedure was stopped after 5 iterations. It was found that the solutions can be further improved with several solution corrections. To do this, the difference between the travel-times calculated using the original checkerboard values (-0.3 and +0.3 km/s) and the travel-times calculated using the solution obtained after 5 LSQR iterations was inverted using 5 LSQR iterations again to obtain the second solution which was used to correct the first solution. Then, the difference between the original travel-times and the travel-times calculated using the corrected solution was inverted and the solution obtained at the previous step was corrected again using the newly obtained solution, and so on. Fig. 7 displays the checkerboard results obtained after three iterative corrections. Fig. 8 illustrates the *RMS* (root mean squares) curves of the travel-time residuals $\Delta\mathbf{T}$ and the obtained velocity perturbations $\Delta\mathbf{V}$ corresponding to these three iterative corrections, where

$$RMS(\Delta\mathbf{x}) = \|\delta\mathbf{x}\| = \sqrt{\frac{1}{n}\sum_{p=1}^{n_p}\delta x_p^2} \quad ; \tag{9}$$

$$RMS(\Delta\mathbf{T}) = \|\delta\mathbf{t} - \mathbf{A}\delta\mathbf{x}\| = \sqrt{\frac{1}{m}\sum_{j=1}^{m}(\delta t_j - \sum_{p=1}^{n_p} a_{jp}\delta x_p)^2} \quad ; \tag{10}$$

and n_p is the number of unknowns (here only velocity perturbations were tested and therefore $\mathbf{x}=\mathbf{V}$); m is the number of equations. Both of the curves have shown good convergence in the iterative procedure. It was found that the results obtained after the three corrections can also be obtained after 21 LSQR iterations. In practice, the observational errors are much larger than the errors in this checkerboard test which are the roundoff errors of the single precision calculation. The LSQR procedure should be stopped after a small number of iterations in real data inversion in order not to involve the smallest singular values. Therefore, this iterative velocity correction is considered to be an efficient procedure for real data LSQR inversion.

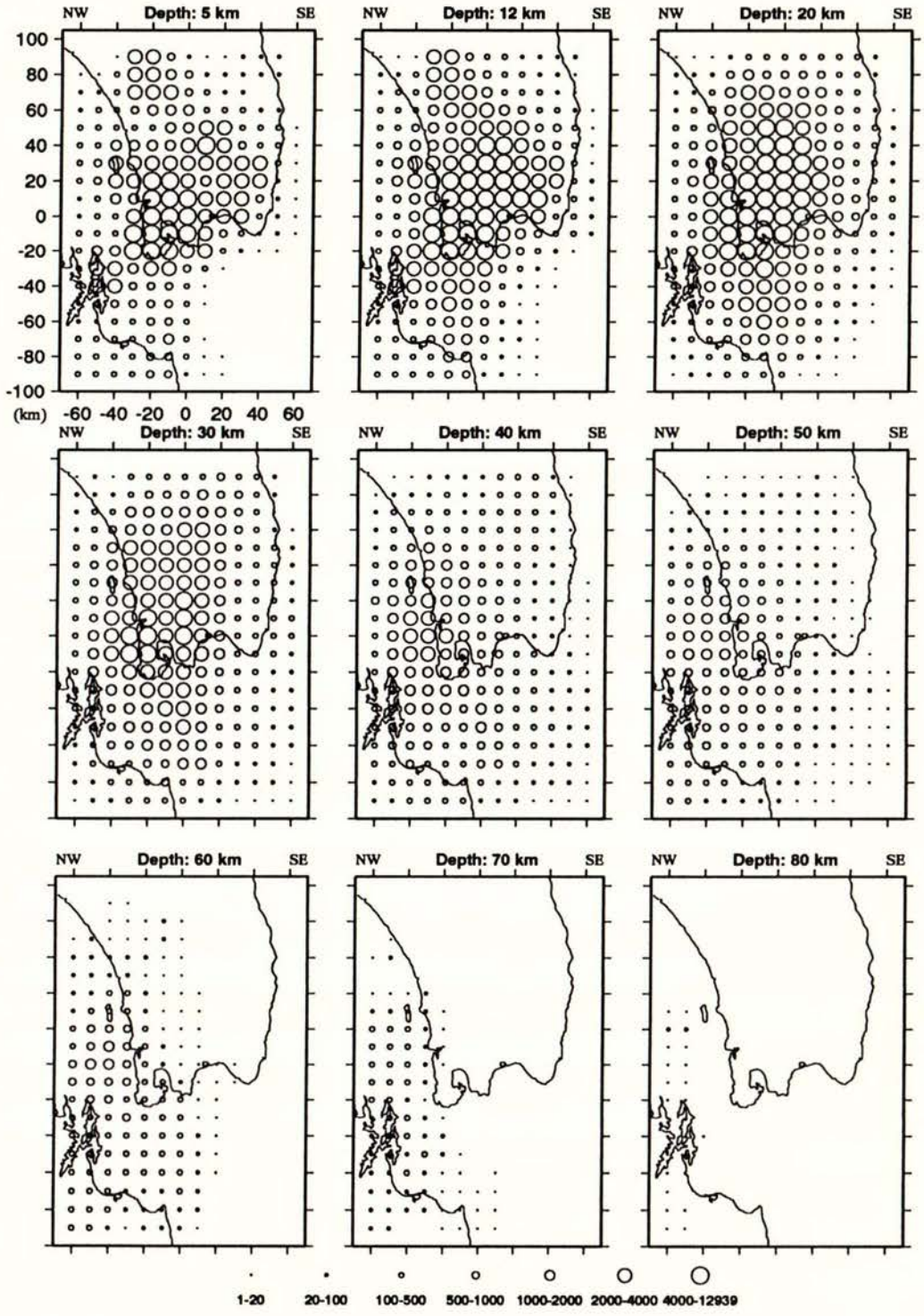

Fig. 6 Hitcounts of velocity grid points of Model A.

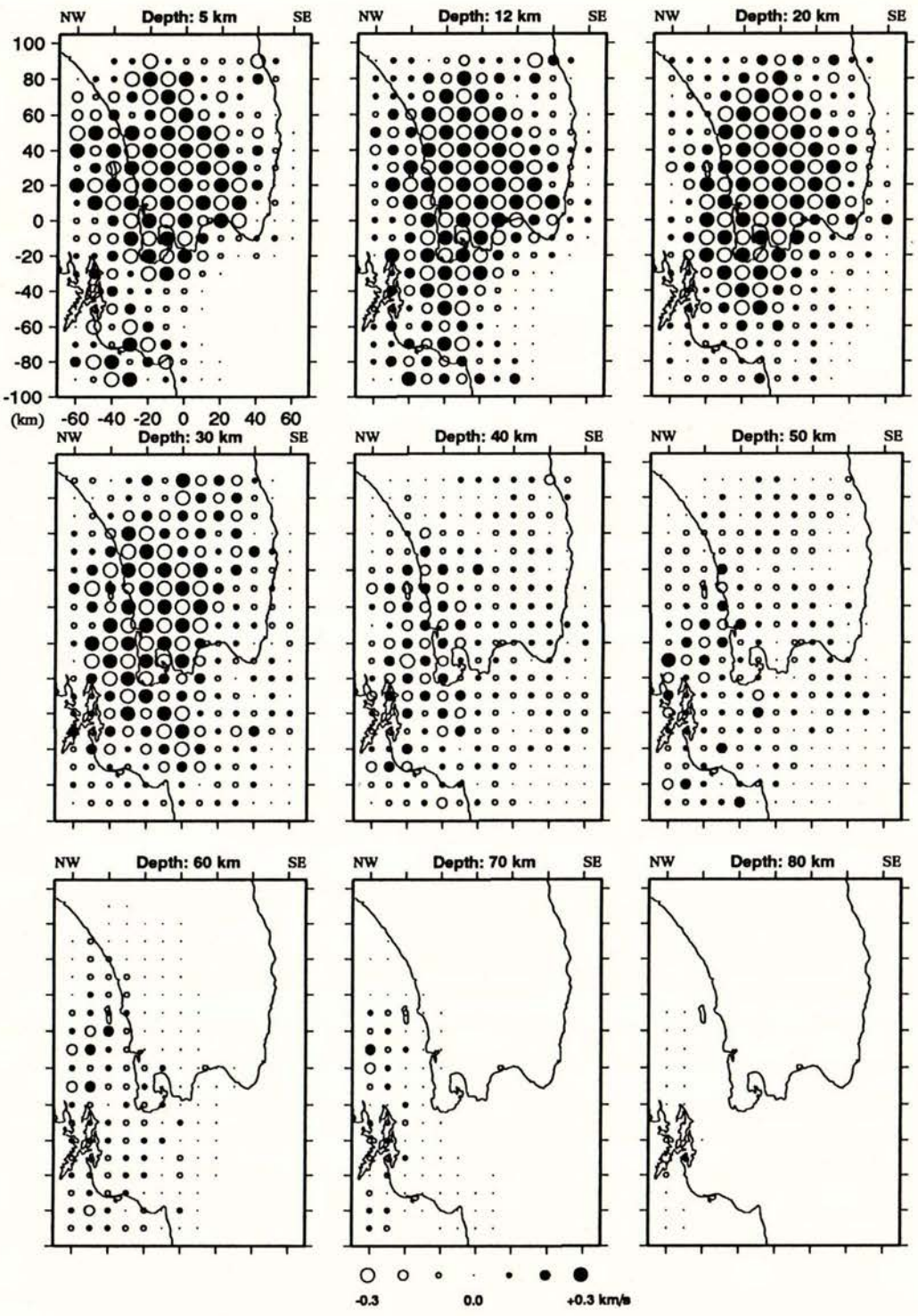

Fig. 7 Results of the checkerboard analysis after three iterative corrections.

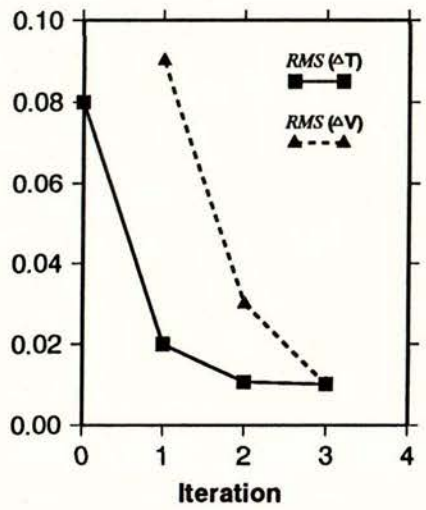

Fig. 8 The *RMS* curves of the travel-time residuals ΔT (in seconds) and the obtained velocity perturbations ΔV (in km/s) corresponding to the three iterative corrections in the checkerboard test.

As seen from Fig. 7, in most of the ray sampled regions at depths of 5, 12, 20 and 30 km, the resolution of the images can reach 10 km horizontally and 7-10 km vertically. However, at the edges of these sampled regions less well resolved solutions were obtained. With increasing depth, the regions with 10 km spaced resolution become narrower and shift towards the northwest, as shown by the diagrams for 40, 50 and 60 km depths. Below 60 km the resolution of the solutions becomes poorer. Another important feature of the results is the amplitude of the velocity perturbations obtained at each of the grid points. The original absolute value of the velocity, 0.3 km/s, can only be obtained at a small number of points. Most of the solution amplitudes are smaller than the original values. Generally, better resolution and more reasonable solutions were obtained in regions which were characterized by good ray coverage. However, for certain less well sampled but well constrained regions, good resolution and good solution amplitudes were still be obtained. This is seen in the small regions near stations CAZ, CCW and GFW (see Fig. 2), where the hit-counts are relatively small (Fig. 7). These regions were found to be sampled well by seismic rays from large variety of directions. Hence, the solutions for these regions were well constrained during the inversion. Poorer resolution and solution amplitude were generally produced at the edges of the ray sampled regions as well as in deeper regions which were poorly sampled by small number of rays from limited variety of directions.

4.6 Real data inversion

The travel-time residual system of the real data obtained on Model A was solved using LSQR. Unlike the previous checkerboard test, the real data inversion involved the simultaneous solution for velocity perturbations, location corrections and station terms. As the travel-time residual system was ill-conditioned and the travel-time residuals were contaminated by observation and model linearization errors, the LSQR procedure was stopped after 5 iterations. Like the inversion procedure used in the checkerboard test, the final results of the real data inversion were obtained after several iterative solution corrections.

Rescaling

As the coefficients of the travel-time residual system composed of parameters with different physical meanings (velocity perturbations, location corrections and station terms) and different magnitudes, rescaling (see section 2.1) on these coefficients was performed. The average absolute values of velocity coefficients was determined to be approximately 0.12, in agreement with the average absolute values of the location coefficients (exclusive of the origin time coefficients) which were found to be approximately 0.13. The coefficient amplitudes of the origin time and the station terms always have the value 1. These coefficients were first rescaled using a constant value 0.13. The inversion of the first rescaled system yielded very small earthquake location corrections, with the maximum correction less than 0.4 km, and small station terms. The incorrect location corrections may cause the portion of the travel-time residuals which are produced by the earthquake mislocations to be interpreted incorrectly as a part of velocity perturbations. As has been discussed previously, unknowns which are poorly sampled by seismic rays will be weighted less heavily in inversion. The location parameters are generally least well sampled by seismic rays. In this model, the maximum sampling rate for the earthquake parameters is 38 (38 arrival times) and the average sampling rate is about 12. The obtained very small location corrections were produced by the less heavy weighting due to the small sampling rate. In order to interpret the location parameters better, the second rescaling using larger values was performed on the location and station term coefficients. However, as the location parameters are less well sampled, they become less well constrained. Using significant scaling for these coefficients may also overweight the location uncertainties and may further affect the final obtained velocity images. It is problematic to determine the correct scaling values for different physical parameters in the LSQR inversion. It was assumed that the hypocentral corrections obtained after rescaling should be close to ± 2.0 km for this case. The rescaling values for location and station term coefficients were obtained empirically using a trial approach. It was found that using different rescaling values on

the location coefficients changed little the pattern of the velocity images but did affect the amplitudes of the velocity perturbations. The greater the rescaling values, the smaller were the resulting velocity perturbations. The final rescaling values were obtained to be 7 for location coefficients and 4 for station terms after the first rescaling.

Weighting

The weighting scheme (see section 2.1) was applied to both P and S travel-time residuals according to their quality factors in order to down-weight the influence of observations of poorer quality. Four weighting values were used in this study and are listed in Table 5.

The same LSQR inversion procedure was used for the solution of the weighted travel-time residual system. The obtained final results were found to be very similar to those obtained without weighting. Rowan and Clayton (1993) have also reported similar results from both weighted and unweighted inversions. It appears that the larger observational errors have been reduced statistically due to using a large number of observations so that the effect of these errors on the inversion results became insignificant. Additionally, each of the LSQR solutions was obtained within 5 iterations, before the smallest singular values became involved. This also prevented the effect of large observational errors on the inversion results. Therefore, using the LSQR inversion procedure which involves only a few iterations, the final solution seems not to be affected significantly by the observational errors.

Table 5 Weighting values used in this study

Weighting Value	Quality Factor	Accuracy (s)	Phases
1.00	0	<±0.10	P, S
0.75	1	±0.10 - ±0.25	P, S
0.50	2	±0.25 - ±0.50	S
0.25	3	±0.50 - ±1.00	S

4.7 The final velocity images of Model A

The travel-time residual system, which was rescaled and without weighting, was solved using the LSQR inversion procedure. The iterative solution correction process was repeated 4 times. Fig. 9,**A** and **B** illustrate the *RMS* curves of the travel-time residuals and the velocity perturbations at the 4 iterations. As seen from the curves, the iterations converged to a stable

solution. The final images of the P-velocity perturbations of Model A, obtained after the 4 iterative corrections, are displayed in Fig. 10. No smoothing has been used for these final images. The final obtained location corrections are all within ±2 km. The obtained station terms are listed in Table 6.

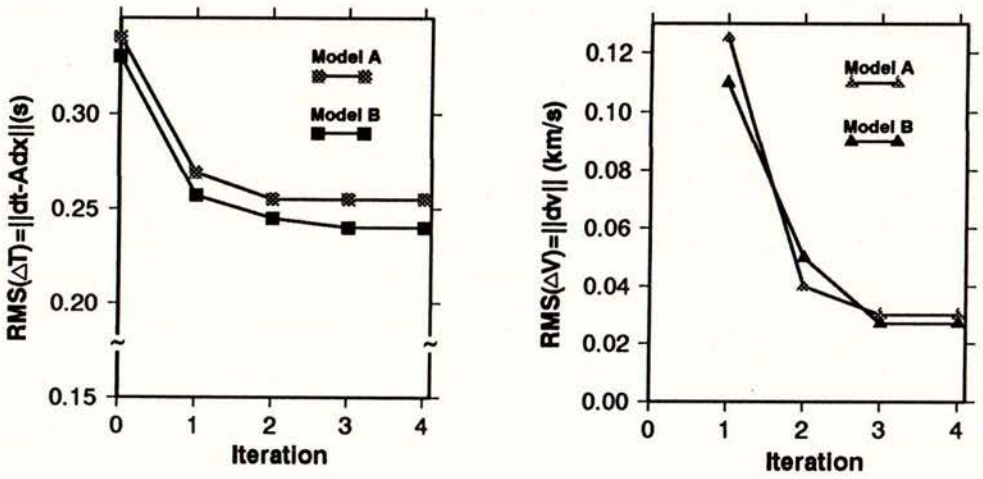

Fig. 9 The *RMS* curves of the travel-time residuals (**A**) and velocity perturbations (**B**) obtained from 4 iterative inversions on Model A and Model B.

4.88 Determination of the subduction interface

The objective of this inversion is to provide a 3-dimensional velocity structure from which a better initial velocity model can be constructed and used for further inversion. As this study region comprises both the overlying Australian plate and the subducted Pacific plate, the main emphasis was placed on constructing the subduction interface from the obtained seismic images.

As seen from Fig. 10, the obtained seismic velocity perturbations reveal significant lateral variation of velocities over the study region. Above 50 km, the velocity distributions appear to be dominated by the northeast trending structures. At the shallowest depth, 5 km, the velocity increases generally from the east coast towards the western margin. This is in agreement with the results of the velocity inversion for the upper Australian crust obtained by Robinson (1986). At 12 km depth, a high velocity region of approximately 20 km in width emerges along the east coast, extending approximately 70 km from Cape Palliser northeast towards the Pacific ocean. At 20 km depth, where are found both the Australian and Pacific plates (Robinson 1986; Ansell and Bannister 1991), a relatively higher velocity region is also found in the upper eastern region. This region becomes wider than that at 12 km and extends further westwards. The velocity perturbation

diagram shows that this high velocity region terminates offshore abruptly south of Cape Palliser. At 30 km depth, the velocity distribution is dominated by a eastern high and a western low velocity zone trending northeast. Compared with the position of the relatively high velocity region at 20 km depth near Cape Palliser, the high velocity region at this depth is much wider and extends further westwards. Because the distribution of these high velocity zones at depths of 12, 20 and 30 km on the eastern side are in very good agreement with the Pacific plate subduction, they should be caused by faster subducting materials. Therefore, the subduction surface should be located in the western front of these high velocity regions. It is difficult to trace the corresponding high velocity regions from the images at 40, 50 and 60 km depths. At 70 and 80 km depths, the resolution is very poor (Fig. 7). Therefore, the inversion results at these two depths are not considered to be meaningful and will not be discussed further.

Table 6 Station terms *(in seconds)* of Model A.

Station	Station Term	Station	Station Term	Station	Station Term
AMW	0.01	MPE	0.01	K05	0.02
BBW	0.00	NDE	-0.01	K07	0.02
BHW	-0.02	PDD	-0.01	K09	0.03
BLW	-0.11	PRE	-0.01	LN1	-0.03
CAW	0.05	RHR	-0.01	LN2	-0.03
CCW	0.01	BBR	0.01	LN3	-0.05
GFW	-0.02	EVR	0.00	LN4	-0.02
KIW	-0.01	HOR	-0.01	LN5	-0.04
MOW	-0.07	PAR	0.02	LN6	-0.02
MRW	-0.02	TGR	-0.02	LW3	-0.04
MTW	-0.04	WBR	-0.01	LW2	0.09
OTW	-0.01	CPE	0.01	LW1	0.03
QHW	-0.09	TAE	0.01	E01	0.00
TCW	-0.06	A11	0.00	E02	0.01
WDW	-0.03	MNT	-0.01	E03	0.01
WEL	0.07	L01	0.01	E04	0.00
MNG	-0.14	L08	0.02	E05	0.01
MRZ	-0.05	PB1	0.01	E06	0.01
CAZ	-0.02	PB7	0.00	E07	0.00
BSE	-0.01	K01	0.01	E08	0.00
HHE	-0.04	K02	0.01	E09	-0.01
KSE	-0.04				

In order to determine the shape of the subduction interface, images of the velocity perturbations on four depth cross sections A-A', B-B', C-C' and D-D', as shown in Fig. 10, are constructed and displayed in Fig. 11. These cross sections are all located in the regions where well resolved solutions have been obtained (Fig. 7). Sections B-B' and C-C' are arranged on the two sides respectively, just beside the termination of the high velocity region near Cape Palliser. D-D' is a cross section approximately parallel to the strike of the subducted plate.

As seen in the images of cross sections A-A', B-B' and C-C', a high velocity structure dipping from southeast down to northwest can be identified clearly and consistently on each of the sections. This dipping high velocity structure was inferred to be the upper part of the subducted plate. A smooth boundary which constrains the top of the dipping structure was assumed to represent the subduction interface between the Australian and Pacific plates. It was found that the shapes and depths of the interface are different on each of the three sections. B-B', the section with the best resolved solutions, has a relatively shallower subduction interface. The shallowest interface was located at a depth of approximately 13 km under CPE. The Pacific plate was determined to be subducted at a very small dipping angle from the eastern offshore down to Cape Palliser (CPE) from where the dipping angle increases to approximately 15°. The subduction interface inferred from section A-A' appears to be deeper than that obtained on B-B', implying that the Pacific plate not only is subducted northwest but also has a small dipping angle towards the northeast. This northeast dipping structure can also be inferred from the other cross sections between A-A' and B-B' or from the front boundaries of the high velocity regions near Cape Palliser at 12 and 20 km depths. A significant change of the interface was found within the 20 km between sections B-B' and C-C'. The inferred subduction interface on section C-C' is approximately 7 km deeper under CPE and 10 km deeper under TCW than that on B-B'. As shown on C-C', the Pacific plate is subducted northwest at a shallow dipping angle of about 6° from the eastern offshore to a depth of approximately 25 km under Wellington city (WEL), from where the dipping angle increases to about 33°. Later, this significant change of the interface between B-B' and C-C' will be shown to be caused most probably by a torn structure in the upper subducted plate. On section D-D' the velocity image shows a rather uniform velocity structure in the subducted plate from 30 km depth downwards and over 200 km from the northeast to southwest on this section. The subduction interface shown on D-D' is the result deduced from three sections A-A', B-B' and C-C'. Fig. 12 illustrates the projections of the used earthquakes which are located within 10 km of each of the four cross sections. It is shown that the inferred interface is generally in good agreement with the uppermost portions of the dipping bands of the earthquake hypocentres.

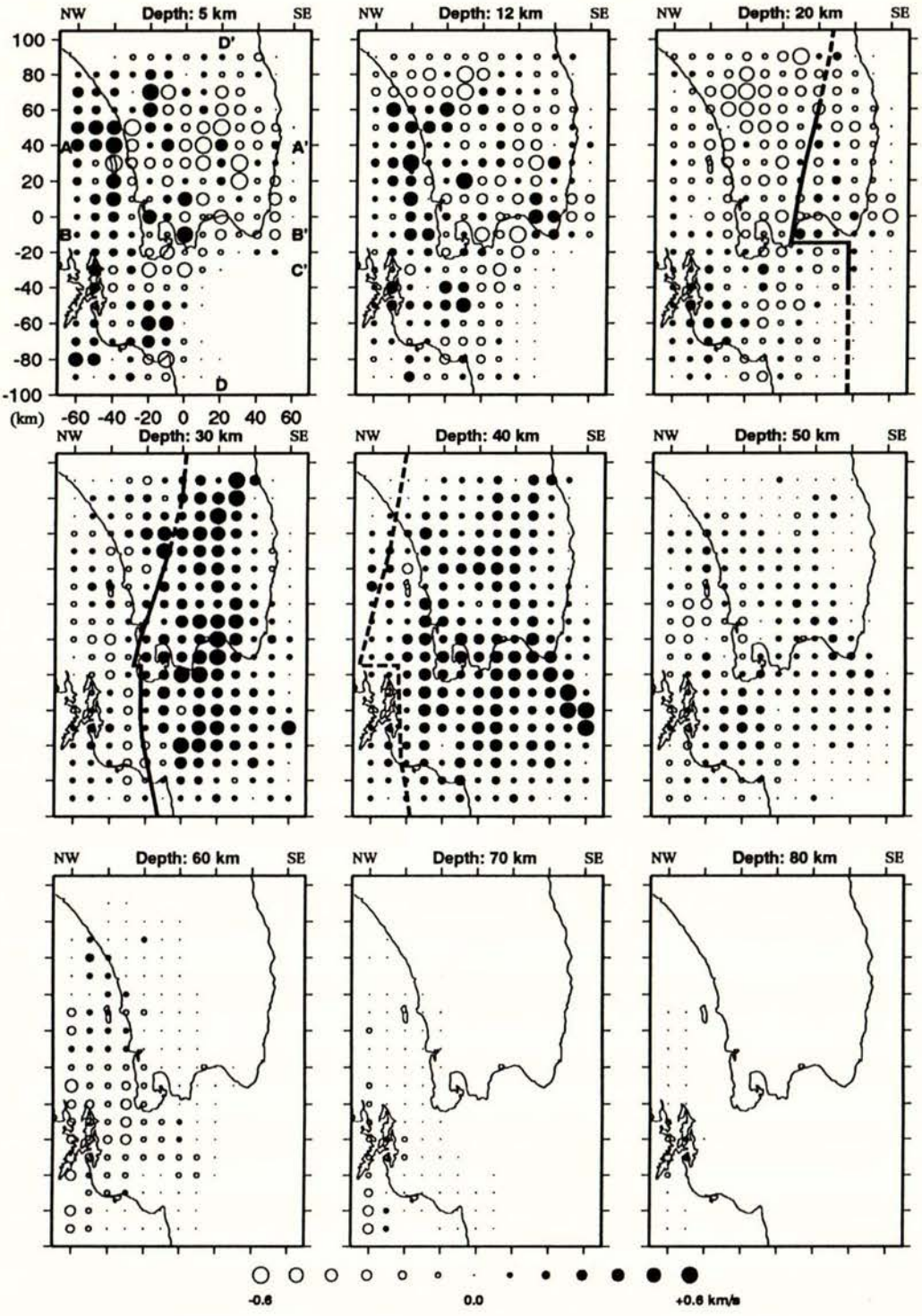

Fig. 10 The images of the obtained P-velocity perturbations for Model A. The bold lines on the 20, 30 and 40 km depth planes represent the positions of the boundary between the Australian plate and the subducted Pacific plate. They are inferred from the velocity distributions of Fig. 11 and the velocity perturbations of this figure. The dashed line sections represent the boundary positions inferred from the less well resolved velocity perturbations.

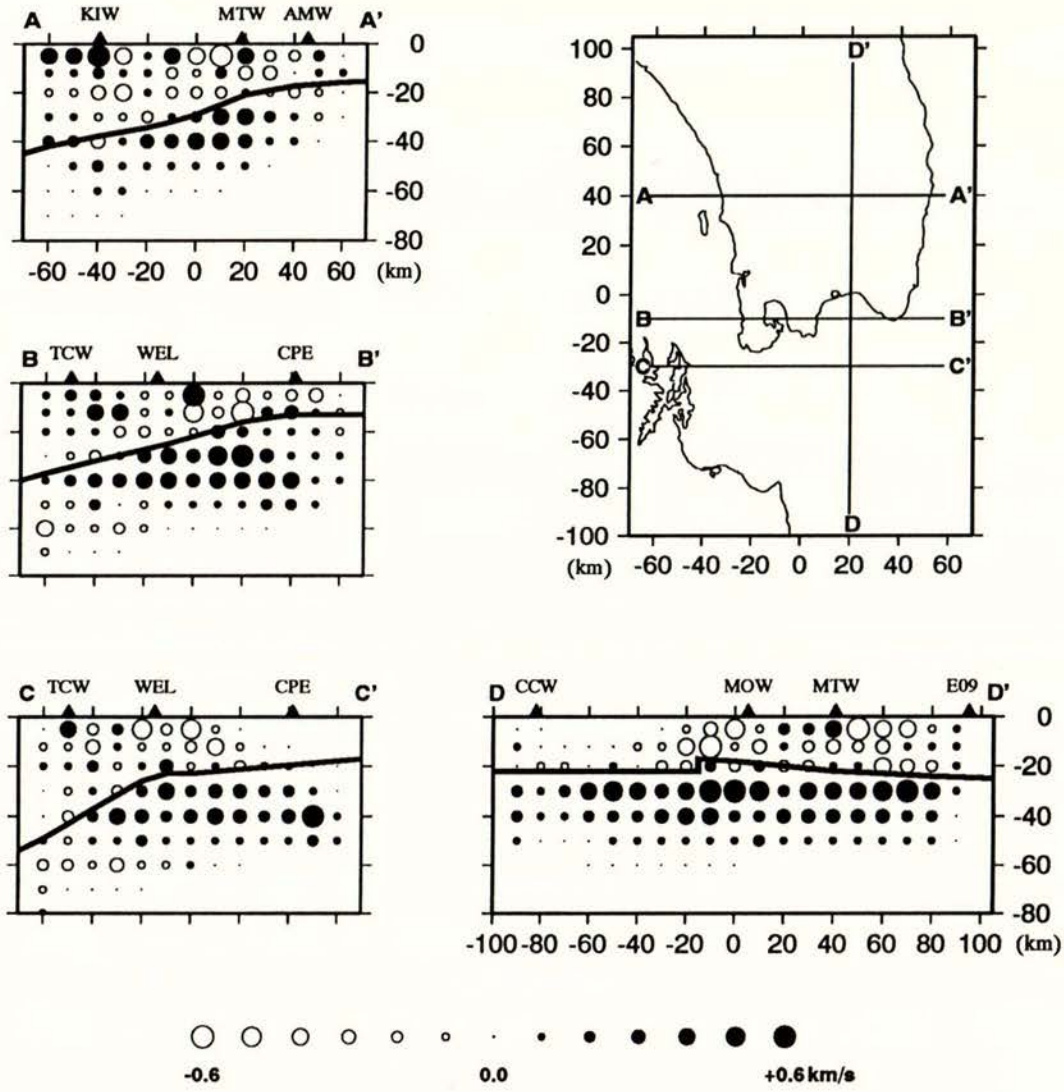

Fig. 11 The obtained velocity perturbations and the inferred subduction interface (bold lines) on four cross sections A-A', B-B', C-C' and D-D' as shown in the 5 km depth plane in Fig. 10.

The inferred subduction interface is also plotted at 20, 30 and 40 km depths in Fig. 10. The boundary curves between A-A' and C-C' are obtained from the deduced boundaries on the A-A', B-B' and C-C' sections. The northeast parts of the boundary curves are extensions of the well determined curves between A-A' and C-C'. Their southwest extensions were determined either by extending the curve (at 20 km depth) or by inferring them from the velocity distribution (at 30 and 40 km depth). Owing to poorer resolution at the western edge of the inversion region, the boundary at 40 km depth may be less well determined.

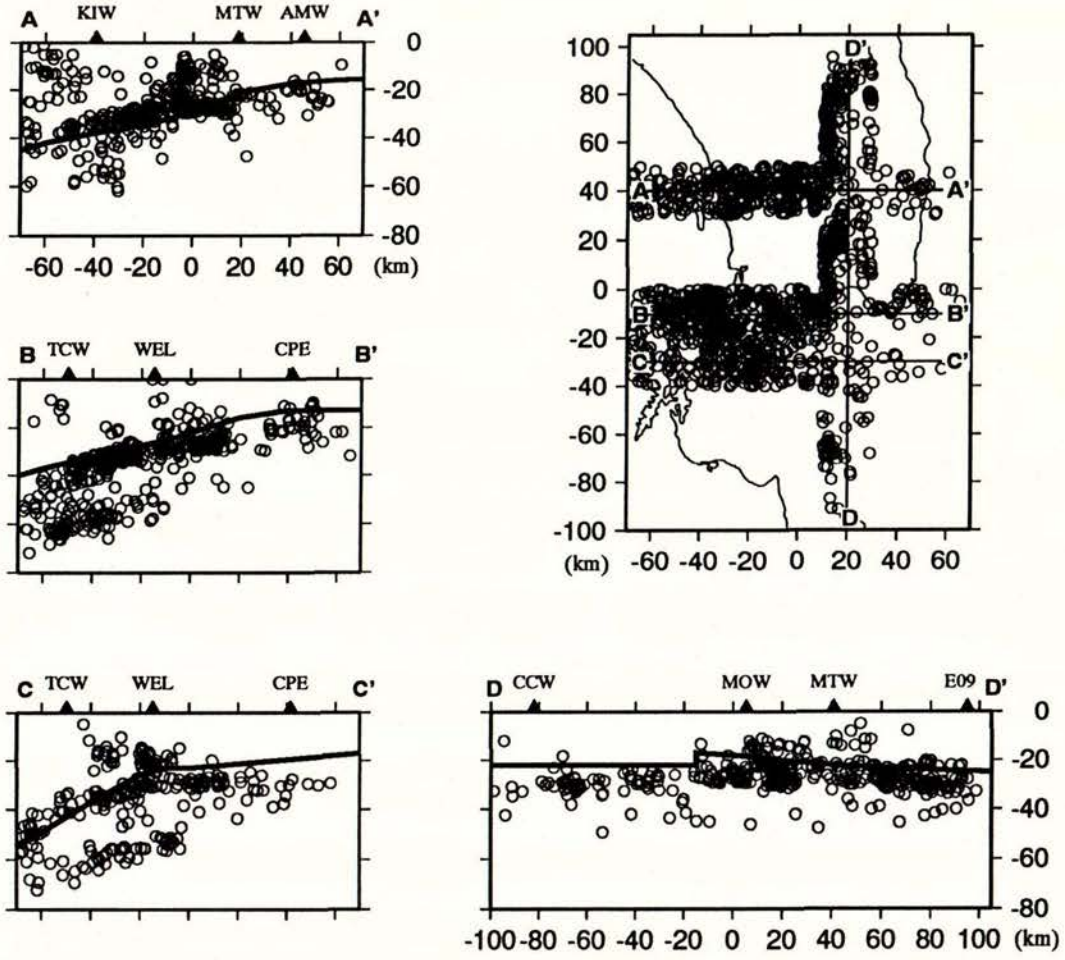

Fig. 12 The epicentres of the earthquakes used in this study which are located within 10 km of each of the four cross sections A-A', B-B', C-C' and D-D', and the projections of the earthquake hypocentres on the cross sections. The bold lines in the four sections represent the subduction interface.

4.9 Initial velocity structure of Model B

Based on the results obtained from Model A, another initial model, Model B, was constructed. This model contained the inferred subduction interface and different initial velocity structures for the Australian plate and the Pacific plate. In order to compare the inversion results of Model B with Model A, the parameterization of Model A was also used for Model B. Fig. 13 illustrates the 3-dimensional view of the inferred subduction interface which was used in Model B. The velocity perturbations obtained from Model A have shown that near the subduction boundary, the velocities in the Pacific plate were in general greater than the velocities in the

Australian plate. A similar result has also been obtained in previous work (Robinson 1986). Therefore, different initial velocities were applied independently to these two plates.

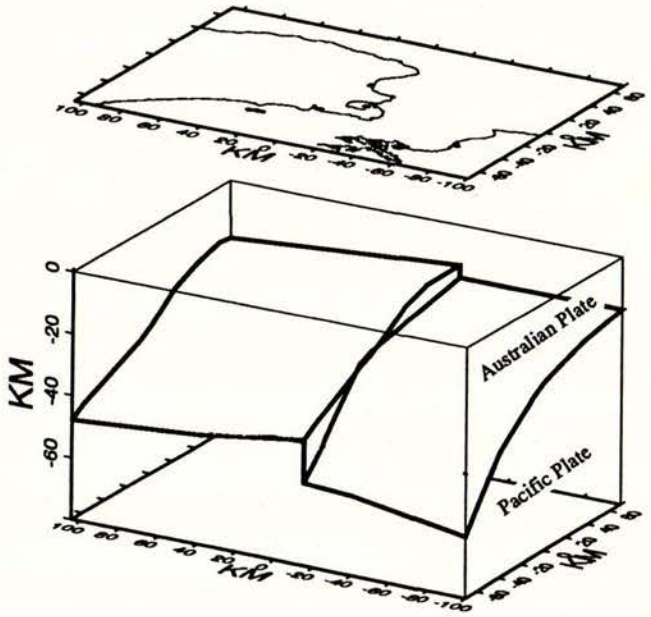

Fig. 13 A diagram illustrating in 3-dimensional view of the inferred subduction interface which was used in Model B.

The initial velocities for the two plates were determined on the basis of the initial velocities of Model A and in reference to the velocities obtained by Robinson (1986) and by Garrick (1968). In the Australian plate, a vertically increasing velocity structure was assumed. The initial velocities of Model A, 5.6 km/s and 6.0 km/s, were also used at 5 and 12 km depths respectively in Model B. The regions in the 20, 30 and 40 km depth planes are shared by both plates. At these depths, the initial velocities of Model B were assumed to be smaller than those in Model A. From the obtained velocity perturbations of Model A, the velocity in the upper subducted crust was found to increase with depth. A uniform upper subducted crust under this region as suggested by Robinson (1986) is therefore considered unlikely to exist. Here, the initial velocities in the Pacific plate were also assumed to vary with depth. At depths 20, 30 and 40 km, the initial velocities were assumed to be greater than those used in Model A. Table 7 lists the initial velocities used for the Australian and Pacific plates in Model B.

Table 7 Initial velocities of Model B

Australian plate		Pacific plate	
Depth(km)	Vp(km/s)	Depth(km)	Vp(km/s)
5	5.6		
12	6.0		
20	6.3	20	6.7
30	6.6	30	7.3
40	7.0	40	8.0
		50	8.6
		60	8.7
		70	8.8
		80	8.8

4.10 The inversion results of Model B

The 40,537 seismic rays from the 3,340 earthquakes used for Model A were also traced on Model B using the 3-dimensional ray tracing method. Approximately 2% of the rays failed to reach their stations because of the problems of either the shadow zone or the divergent target searching. A travel-time residual system containing 39,646 equations was set up for Model B.

Hitcounts were also used to represent the seismic ray coverage for this model. As less seismic rays were used, the hitcounts at some velocity points on Model B were smaller than those on Model A. The maximum hitcounts at a point in Model B was 12,743; by comparison, the maximum for Model A was 12,939. The hitcount patterns obtained on Model B are shown in Fig. 14, which are very similar to those obtained on Model A over most of the study region. In the vicinity of the subduction boundary, Model B has smaller hitcounts. This is because the velocity interpolation during the ray tracing only used the initial velocities at the grid points which were close to and located in the same velocity block as the interpolated ray point. Because there was no velocity discontinuity in Model A, that study region was treated to be a single velocity block. Thus, in Model A the velocity of any ray point was interpolated using the initial velocities close to it. However, once the interface was placed in Model B, the study region was divided to two velocity blocks. In this case, the velocities on the other side of the interface cannot be used for the interpolation for this ray point. This produced smaller ray sampling rates at the velocity points which are close to the boundary in Model B.

The checkerboard test was carried out for Model B using the same original checkerboard values and the same approach as used previously for Model A. The final inversion results of the checkerboard test are displayed in Fig. 15. Compared with the checkerboard results of Model A

(Fig. 7), good resolution was also obtained on the planes at depths above 50 km in Model B. However, the obtained values at the velocity points near the subduction boundary become generally smaller. This is in agreement with the distribution of the hitcounts (Fig. 14). It was found that the amplitude of an obtained unknown value depends upon the sampling rate of seismic rays on this unknown seriously. The original checkerboard values were generally well recovered at the points which had the greatest sampling rates. Smaller values were always obtained at points located in the edges of the inversion region and in the vicinity of velocity boundaries, where smaller sampling rates occurred. This deficiency seems to be unable to be removed using any of the present inversion methods and appears to be more serious when LSQR inversion is used. The rescaling scheme suggested by Pulliam et al. (1993) was used for the velocity coefficients, but no satisfactory results were obtained. In this study, the final inversion results were all obtained without rescaling the velocity coefficients.

The inversion procedure for Model B was as same as that for Model A. The subduction interface was fixed throughout the inversion procedure. Fig. 16 displays the final obtained velocity perturbations on Model B. The *RMS* curves of the travel-time residuals ΔT and the velocity perturbations ΔV, corresponding to the four iterative calculations are illustrated in Fig. 9. It shows that using the new initial model the *RMS* of the travel-time residuals is reduced by approximately 6% from 0.255 s to 0.240 s. The obtained earthquake location perturbations and the station terms are very similar to those obtained for Model A. At the depths of 5, 12, 50, 60, 70 and 80 km, the obtained velocity perturbations show very similar patterns to the those of Model A. It appears that putting in a subduction interface and changing the initial velocities at 20, 30 and 40 km depths in the two plate regions did not change the inversion results in the other regions significantly. Taking the initial velocities into consideration, the velocity perturbations in the 20, 30 and 40 km depth planes also have relatively higher velocity values in the Pacific plate. However, these high velocity regions cannot be identified directly from the final images of Fig. 16 without referencing the initial model. It is unsuitable to represent the velocity distributions by summing the velocity perturbations and the initial velocities. This is because the velocity perturbations which were determined at the well sampled points are mixed with the perturbations which were produced by less frequent sampling. The summation of the velocity perturbations and the initial velocities may produce artifacts to the velocity results. Therefore, no any further processing on the final images of Fig. 16 was performed. As Model B produced the solutions correspond to smaller *RMS* travel-time residuals, it becomes the preferred model for interpretation.

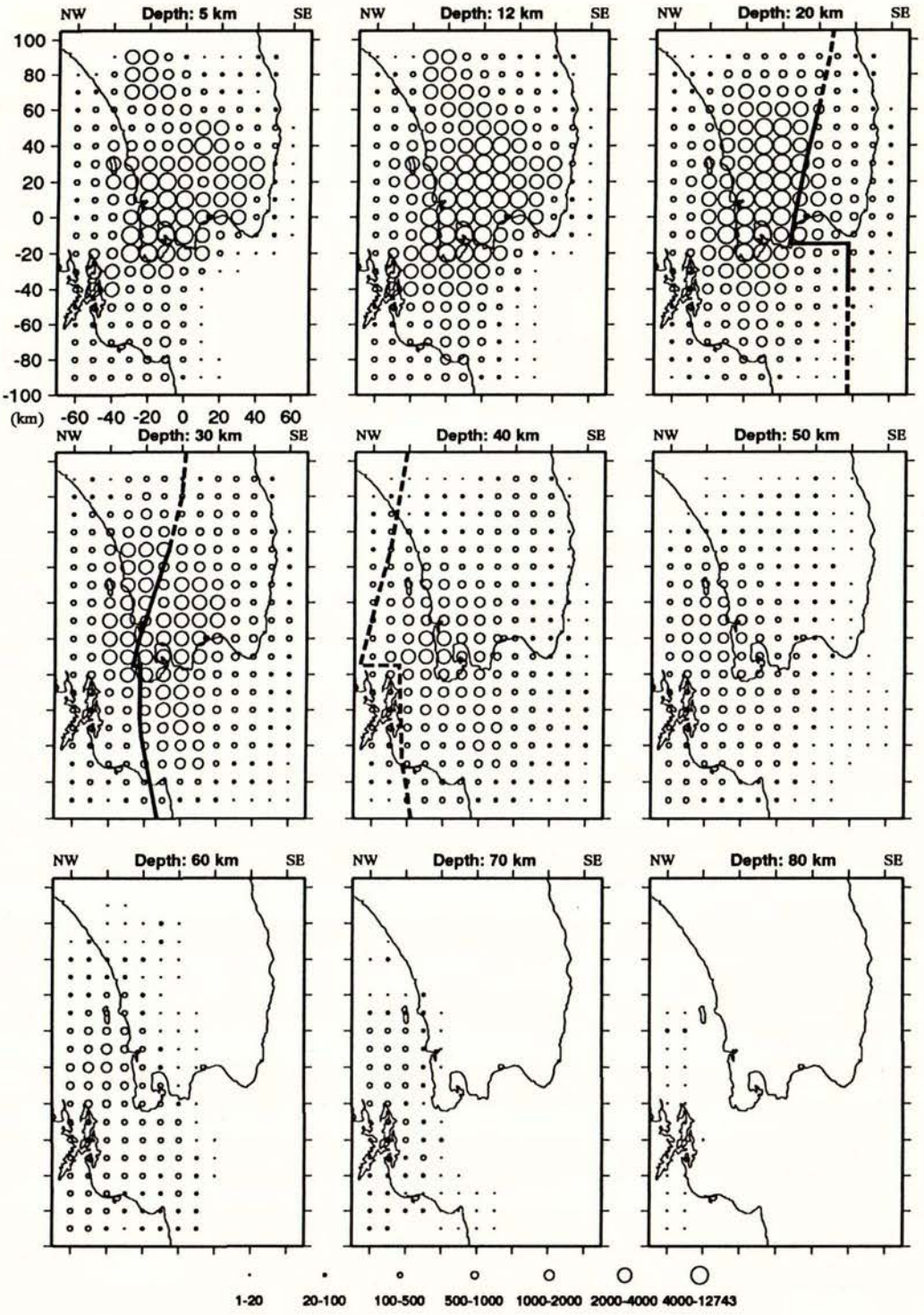

Fig. 14 Hitcounts of velocity grid points of Model B.

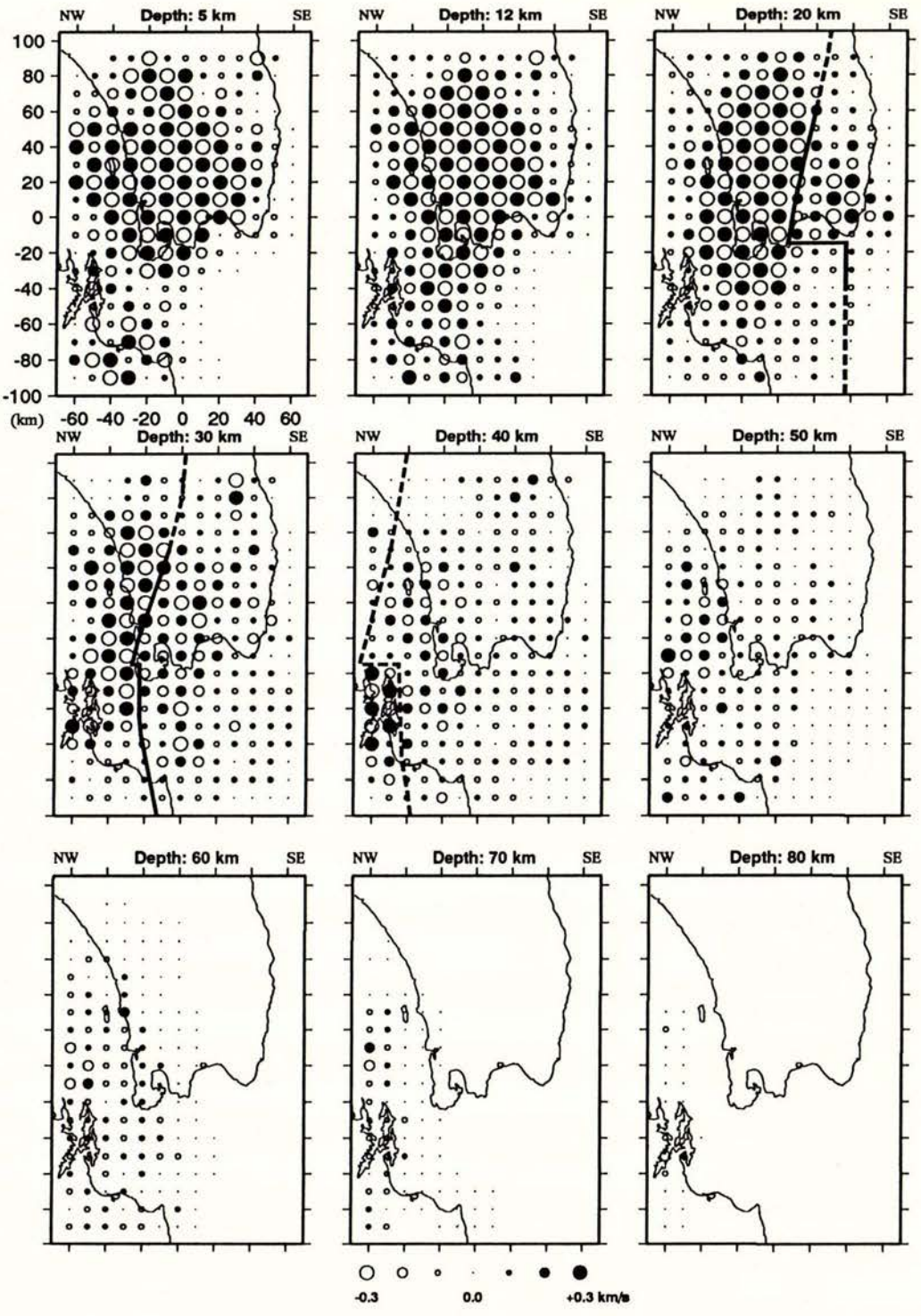

Fig. 15 Results of the checkerboard analysis of Model B, obtained after three iterative corrections.

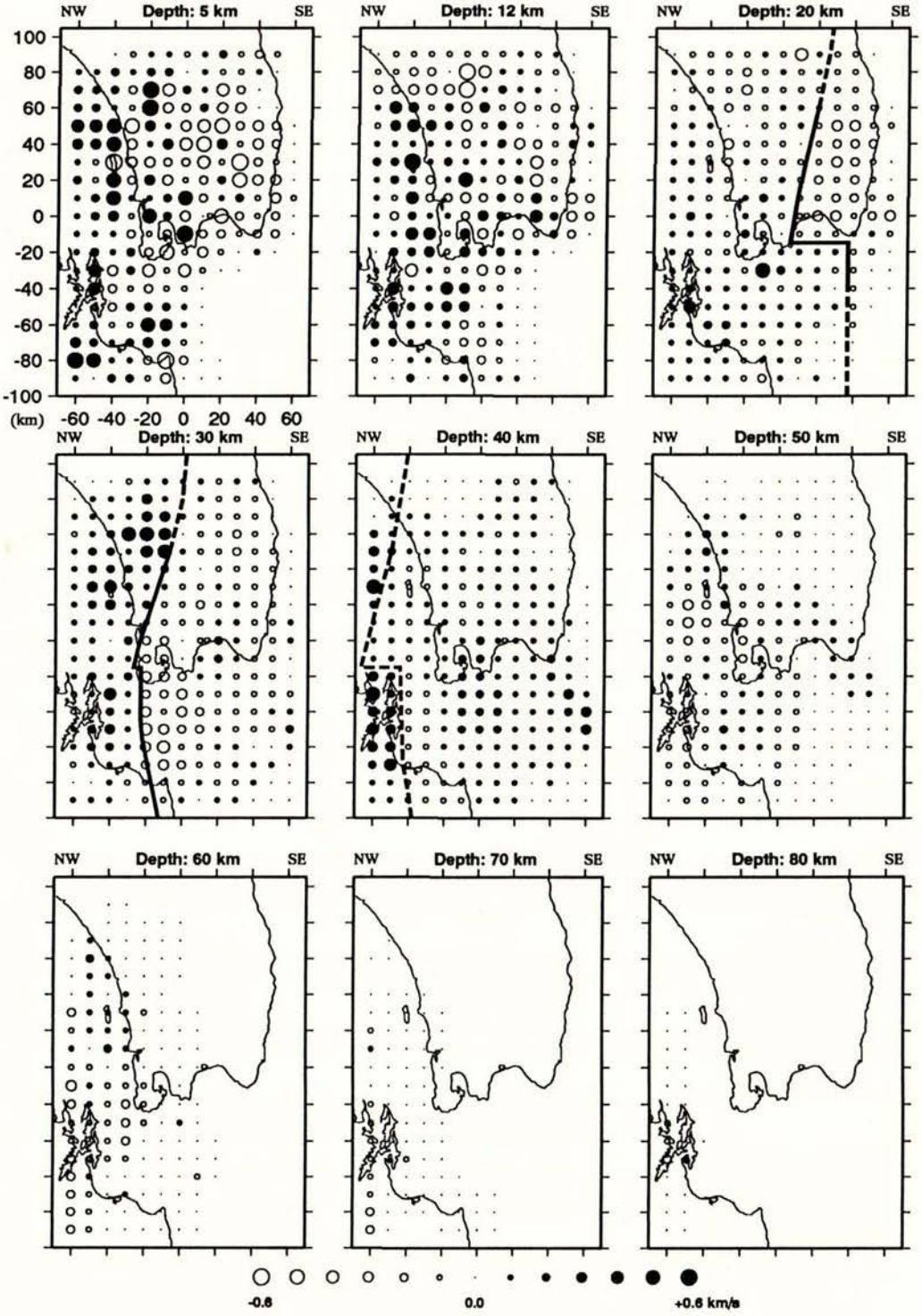

Fig. 16 The images of the obtained P-velocity perturbations for Model B. The bold lines in 20, 30 and 40 km depth planes are the subduction boundary between the Australian plate and the Pacific plate. They were inferred from the results obtained on Model A. The dashed lines represent the boundary positions inferred from the less well resolved velocity perturbations.

5. DISCUSSIONS

5.1 Velocity structures in the Australian and Pacific plates

The obtained velocity perturbations reveal significant variations in P-wave velocity in the crust of the Australian plate (Fig. 16). Above 20 km, the velocities generally increase from the east coast towards the western edge. This is in agreement with the result obtained by Robinson (1986). At the shallowest inversion depth, 5 km, the velocity perturbations appear to have good correlations with the geological structures exposed on the ground surface (Fig. 1). On the North Island, three velocity regions can be identified. The region to the east of the Wairarapa Fault, dominated by low velocities, corresponds mainly with the Cenozoic sedimentary rocks on the surface. Offshore of east Cape Palliser lies a lower velocity region which extends to a depth of about 12 km. This low velocity region is consistent with the low velocity structure offshore of east Cape Palliser obtained by Luo (1992) using multiple seismic phases. As the amplitudes of these low velocity perturbations are not fully recovered in this seismic tomographic inversion due to less frequent seismic ray sampling, the true velocity values cannot be obtained from this work for this region. In reference to the results of the checkerboard test (Fig. 15), the obtained values are much smaller than the original values in this region. This suggests that the velocity at 12 km depth east of Cape Palliser is lower than 5.70 km/s which is obtained from the summing of the perturbations and the initial value and perhaps correlating with the low velocity of 5.0 km/s obtained previously in this region (Luo 1992). This low velocity structure may correspond to the accreted or underplated sediments of accretionary margins described by Davey et al. (1986). The second velocity region, lying between Kapiti Island and the Wairarapa Fault, is characterized by a mixture of high and low velocity perturbations. Pervasively distributed Jurassic greywacke and Quaternary sediments have been found on the surface in this region. The low velocity perturbations, extending northeast along the west coast, are in very good agreement with the distribution of the Quaternary sediments. To the west of Kapiti Island, a substantial high velocity zone can be traced consistently down southwest to the South Island where Triassic schists are exposed. This high velocity zone appears to extend downwards to at least 20 km depth.

On the South Island, the western high velocity zone is strongly correlated with the Triassic schists on the western side of the Wairau Fault. The low velocity perturbations near Cape Campbell are overlain by Quaternary sediments. The Cook Strait is characterized by nearly square regions of both high and low velocity perturbations. Offshore of Wellington city is located a low velocity block of dimensions 30×30 km approximately. A high velocity region with similar dimensions is located just between the low velocity block and the low velocity perturbations of Cape Campbell. The changes of these velocities are shown to be abrupt. This implies that

significant variations in rock properties and faulting structures may exist in the upper Australian plate under Cook Strait. The distributions of these velocity boundaries suggest that faults in NE-SW and NW-SE trends may dominate in the Cook Strait crust.

At 12 km depth, a high velocity region of approximately 20 km in width also exists near Cape Palliser along the east coast, above the inferred subduction interface. This region appears to extend approximately 70 km northeast towards the Pacific ocean and to contribute to the highest Bouguer gravity anomaly of approximately 900 μN/kg observed in this region (Ivory 1986). As the southern termination of this high velocity body is found at the location where the torn structure of the subducted plate occurs (see later discussion), it may have been formed by the subducting process and controlled by the subduction structure. It appears to require large rock bodies with faster P-wave velocities than the surrounding rocks above the inferred subduction interface in order to produce this high velocity structure. One possibility is that this might be produced by a horst-like structure in the subducted crust as proposed by Barnes and Korsch (1991). A schematic diagram of this structure is given in Fig. 17,**A**. As intrusions of volcanic rocks have been observed and shown to be extensively developed along the east coast from Cape Palliser to Tora (Moore and Speden 1979; George 1988; Barnes 1990) and continuing basic volcanism has been suggested to have occurred in the Early Cretaceous (Moore and Speden 1979), intrusion of large volcanic rocks in the bottom of the Australian plate along the east coast might be another possibility (Fig. 17,**B**). In the western region at 12 and 20 km depths, the high velocity zone seen at 5 km depth is also found. In Cook Strait, the high velocity body identified at 5 km depth shifts approximately 10 km to the north at 12 km depth. The low velocity region offshore south of Wellington city becomes narrower to approximately 10 km in width before disappearing at 30 km depth.

As seen in Fig. 16, the velocity structures obtained for the Pacific plate are relatively simpler than those obtained for the overlying Australian plate. Generally, at same depth, the velocity in the upper portion of the Pacific plate is greater than that of the overlying plate on the other side of the subduction interface. It is found that the upper portion of the subducted plate is not uniform but increases with the depth under this region. The velocity perturbations in the northern and southern regions beside the torn structure under Cook Strait appear to be quite different. As shown in 30 km and 40 km depth planes in Fig. 16, the velocity increases from the top of the subducted plate to the deep plate in the southern region. However, this increase cannot be found in the region north of the torn structure. The differences of the initial velocities assumed for 30 and 40 km depths (Table 7) between the Australian plate and the Pacific plate are found to be exaggerated by comparison with the inversion results which show that the positive perturbations were always obtained on the western Australian plate.

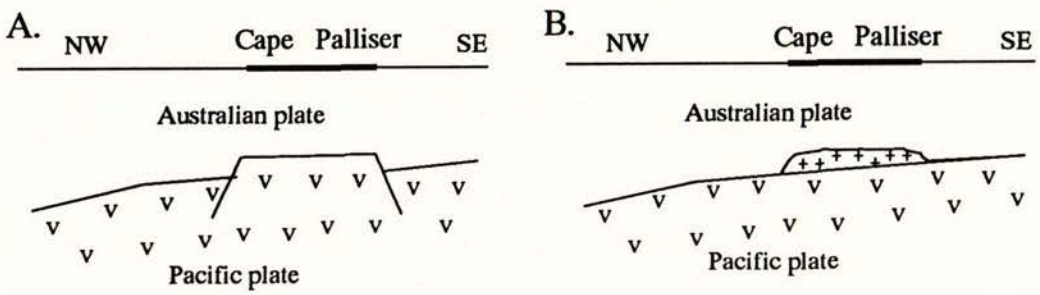

Fig. 17 Schematic diagram showing two possible structures which might produce the high velocity perturbations along the east coast of Cape Palliser as shown in Fig. 16. **A.** shows a horst-like structure in the subducted crust, modified from Barnes and Korsch (1991). **B.** is an intrusion of faster volcanic rocks under the bottom of the overlying plate, deduced from the extensive intrusion of volcanic rocks observed in this region (Moore and Speden 1979; George 1988; Barnes 1990).

5.2 The northern extension of the Wairau Fault

The Wairau Fault (Fig. 1) is thought of as the northern extension of the Alpine Fault (Bibby 1976), and recognized to be a major structural and geomorphic discontinuity between the western side Late Paleozoic schists and the eastern side Jurassic greywacke-floored basin of the Wairau Plains with its fill of the Cenozoic sediments. The northern extension of the Wairau Fault across Cook Strait has long been a point of contention (Robinson 1986; Carter et al. 1988). On the basis of onshore geomorphological trends, the interpreted seabed morphology and geological deformation, the northern extension of the Wairau Fault has been depicted as running northeast across Cook Strait, offshore of east Marlborough Sounds and then offshore along the west coast of the North Island to the east of Kapiti Island (Fleming and Hutton 1949; Wellman 1956; Suggate 1963; Stevens 1974; Suggate et al. 1978). Relying on seismic reflection data, Carter et al. (1988) has located the extension to the west of Kapiti Island, in agreement with the result of Katz and Wood (1980). However, using offshore seismic surveys, Ghani (1974) has found that the Wairau Fault appears to connect with the Wellington Fault. From the result of plate motion reconstructions, Walcott (1978a) has suggested that the Wairau Fault or its ancestors may be bent eastwards offshore towards the east coast of the North Island. These solutions are illustrated in Fig. 18. The uncertainty concerning the extension of the Wairau Fault across Cook Strait and through the North Island derives largely from the lack of any considerable contrast in certain rock types

similar to that which is so prominent in the South Island. Seismic surveys in Cook Strait have not been able to provide reliable information on deeper structure of the northern extension of the Wairau Fault.

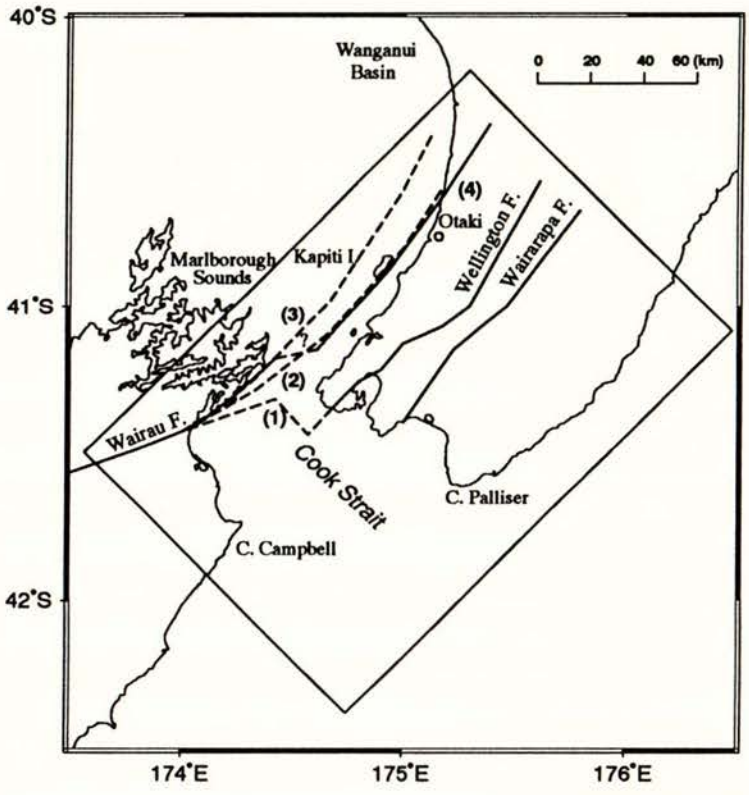

Fig. 18 Solutions of the northern extension of the Wairau Fault. (1) from Ghani (1974); (2) from Fleming and Hutton (1949), Wellman (1956), Suggate (1963), Stevens (1974), Suggate et al. (1978); (3) from Carter et al. (1988), Katz and Wood (1980) and (4) from this study.

The velocity perturbations obtained from seismic tomographic inversion show a very distinct velocity boundary which passes through between Kapiti Island and the west coast at 5 km depth (Fig. 16). To its east lies a narrow low velocity zone which extends northeast. To its west is an extensive high velocity zone, also extending northeast. This high velocity zone is overlain by the southeastern portion of the Wanganui Basin where 1-2 km thick sedimentary rocks have been formed since the Pliocene (Stern et al. 1992a). As most of the earthquakes occurred in Wanganui Basin and used in this study were deeper than 2 km and the seismic stations were all deployed onshore, seismic rays traveled mostly through deeper basement regions, rather than through the

sediments. Hence, the high velocity perturbations correspond to the higher velocity basement rocks under the basin sediments. Extending south, the high velocity zone can be traced consistently to the top of the South Island, where the Triassic schists exist. These schists have been found to have higher seismic velocity (Robinson 1986). Significantly, the location of the velocity boundary at the top of the South Island is in very good agreement with that of the Wairau Fault. This suggests that the high velocity zone at the top of the South Island may be produced by the schists and the velocity boundary corresponds to the Wairau Fault. Based on the seismic refraction results, Officer (1959) suggested that the schists exposed west of the Wairau Fault may extend further northeast for some distance. In a borehole located in the Wanganui Basin, schist has been found at approximately 2.5 km depth (Anderton 1981). This implies that schists may be pervasively distributed in the west of the study region. The consistently high velocities in the western region are most probably correlated with these schists. The velocity boundary is then considered to be the boundary between the western schists and the eastern rocks and the Wairau Fault is therefore considered to continue from the top of the South Island, northeast along the velocity boundary.

As seen from the velocity perturbations at 5 km depth in Fig. 16, the Wairau Fault appears to extend 45° northeast, for approximately 50 km along the east coast of the Marlborough Sounds before being offset or bent sharply near the western offshore of the Wellington Peninsula, from where the fault extends continuously further northeast offshore of the west coast. Based on the distinct velocity boundary, this fault is located to the east of Kapiti Island, in agreement with those earlier reported results (Fleming and Hutton 1949; Wellman 1956; Suggate 1963; Stevens 1974; Suggate et al. 1978). The Wairau Fault appears to extend onshore at northwest of Otaki and further northeast. This extension is also in very good agreement with the trends of the gravity gradient belts offshore of the Marlborough Sounds and along the west of the southern North Island (Ivory 1986). The presumed offset or bent structure of the Wairau Fault occurs near the location where the torn structure of the this subducted plate exists. This suggests that this offset or bent structure may correlate with the development of the torn structure. From the obtained seismic velocity images, the high velocity zone in the western region can be traced down to at least 20 km, indicating that the Wairau Fault may cut down to at least as deep as 20 km. This large scale fault becomes probably a major lithologic boundary in this region and may have fundamentally controlled the development of the basins to its west. The extension of the Wairau Fault obtained from the seismic images is illustrated in Fig. 18. However, the contrasts of velocity perturbations close to two other major faults, the Wellington Fault and the Wairarapa Fault, are not as strong and not as regularly aligned as those beside the Wairau Fault. It is difficult to locate these two faults directly from the obtained velocity perturbations.

5.3 Segmentation of the subducted crust beneath Cook Strait

Segmentation has been suggested in the subducted Pacific plate (Carr et al. 1973; Spence 1977; Reyners 1983; Ramón Cabré 1983; Robinson 1986; Niazi and Karageorgi 1992). The existence of segmentation in the subducted Pacific plate was first proposed by Reyners (1983). On the basis of significant change in seismic mechanisms between the southern North Island and the northern South Island, he speculated that a torn plate may exist beneath Cook Strait region and the segment structure was assumed to be oriented NW-SE and located across the top of the South Island. A further study, using earthquake hypocentres in the two regions on each side of Cook Strait, has found that the northwest dipping subducted plate is approximately 5-10 km deeper south of Cook Strait (Robinson 1986). This big change in depth was suspected to be caused by a torn structure in the subducted plate (Robinson 1986, 1991).

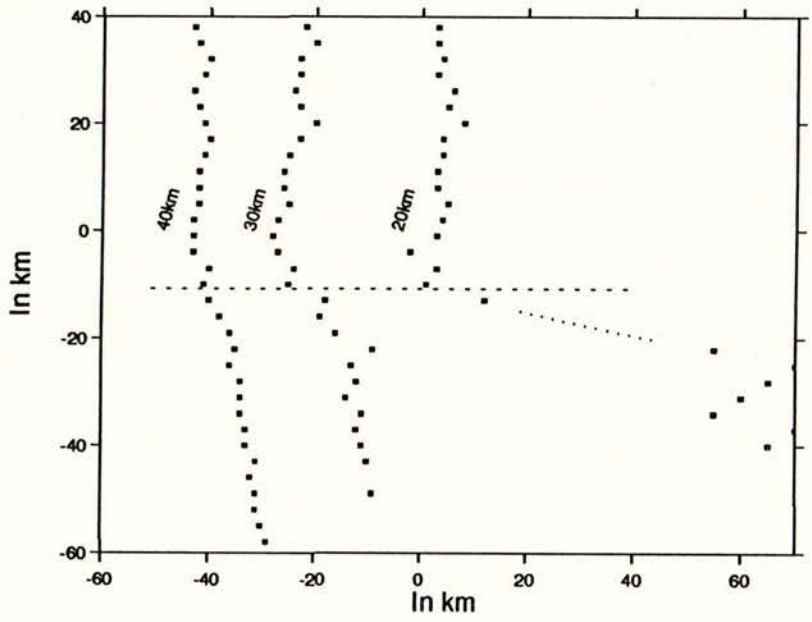

Fig. 19 Depth distribution of the top seismicity envelopes at 20, 30 and 40 km, obtained from 3 km spaced N45°W cross sections across the Wellington region. The horizontal dashed line represents the section across Wellington city running from east to west.

The subducted interface obtained from seismic velocity images shows a significant change in depth across Cook Strait. The depth displacement was found to be approximately 7-10 km deeper under Cook Strait than under the southern North Island and this is occurred over 20 km.

This depth variation is in good agreement with the result obtained by Robinson (1986) from the distribution of earthquake foci, but the resolution of the displacement location is greatly improved in this study. Fig. 19 plots a depth distribution of the top seismicity envelopes obtained from 3 km spaced N45°W cross sections across the Wellington region. These earthquakes occurred during the period 1/1978-7/1993 and were located using Robinson's 2-dimensional velocity model (Robinson 1986). The coordinate system in this figure is the same as that used in Fig. 16. As seen in this figure depths deeper by 6-9 km occur southwest of Wellington city, which is crossed by the dashed line running from east to west. The question can be raised as to how the subducted plate really changes across Cook Strait. Is it steeply deformed or broken into two pieces? A 3-dimensional finite-difference flexural analysis (Stern et al. 1992b) was used to check the possible reasons for the plate displacement. This analysis tests the equilibrium vertical displacement of a horizontal elastic sheet under a load.

From Walcott (1970) the lithosphere is generally treated either as an elastic or a viscoelastic plate overlying the asthenosphere. The old and rigid subducted crust under Cook Strait was modeled as a thin elastic sheet. As we were only interested in its lateral flexural deformation along the east coast, this elastic sheet was treated as flat (Fig. 20) and being driven by a down-load stress on one half (the southern part) and an uplift-load on the other half (the northern part). divided into a grid of squares, each 10 × 10 km. The edge which represents the front of the subduction plate was assumed to be a 'free edge' in the sense that minimal shear stresses are transmitted across it. Two edges representing the southern and northern ends were also allowed to be 'free edges' in order to produce displacements similar in pattern to the obtained displacements. The remaining edge to the east of the Hikurangi Margin was assumed to be continuous. The real stress distribution in a subducted plate may be very complicated. A simple representation of the distribution is usually assumed so that the deformation of the plate can be modeled (Walcott 1970, McNutt et al. 1988, Stern et al. 1992b). Uniform down-load and uplift-load stresses in vertical directions were assumed to simplify the real stress. A buoyant restoring force which separately affects the deformation of an elastic sheet for a given load (Walcott 1970, McNutt et al. 1988, Stern et al. 1992b) was considered in this model. This force depends on the density contrast of the material above and below the flexed sheet. The density of mantle material was assumed to be 3300 kg m^{-3} and 2800 kg m^{-3} was assumed to be the average density for the sediments lying above, giving a restoring force of 5×10^3 Pa per meter (3300-2800 kg m^{-3}) of vertical displacement. A Young's modulus of 1.0×10^{11} and Poisson's ratio of 0.25 were assumed for the sheet.

The deformation of the central elastic sheet (C-C' in Fig. 20) under the given loads is illustrated using deformation curves in Fig. 21. Under a given stress the flexural deformation is

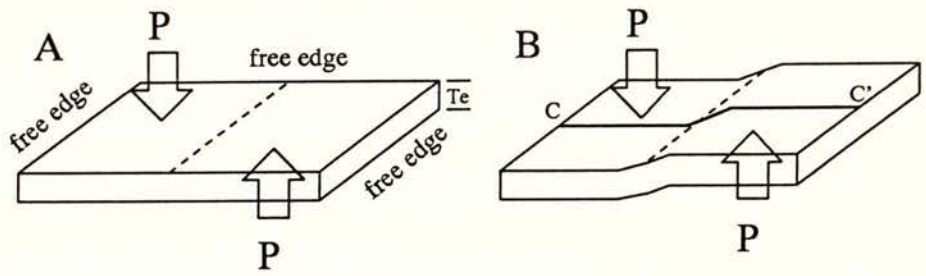

Fig. 20 Sketch of the elastic model for deformation analysis of the subducted plate under Cook Strait as seen from the Hikurangi Margin. A down-load stress, **P,** and an uplift-load stress, **P**, were assumed and exerted uniformly on each of its halves (the southern part and the northern part) respectively. The dashed line is assumed under the north of Cook Strait. In Fig. 20,**A** Te is the thickness of the elastic sheet which is also considered as flexural rigidity of the sheet. Three edges of the sheet are set 'free' (see context). **B,** shows the equilibrium vertical displacement of the sheet under loads. C-C' represents the deformation curve in the centre across the sheet.

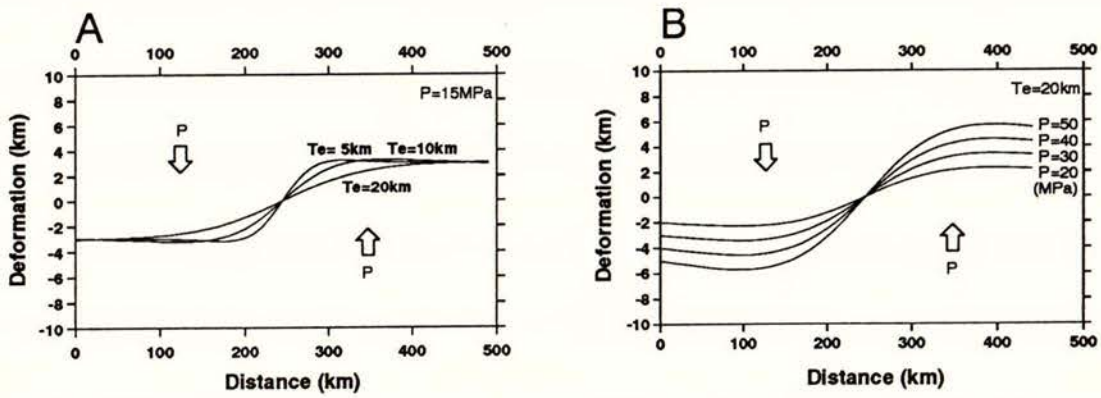

Fig. 21 Deformation curves along the line C-C' of the elastic sheet (Fig. 20) under the given loads. **A,** shows the deformations of elastic sheets in different thicknesses under the same loads. **B,** shows the deformations of a 20 km thick sheet under increased loads.

affected by the thickness of the sheet alone. The thinner the sheet the higher the curvature of the deformation produced. As shown in Fig. 21,**A** the required displacement of approximately 7 km is reached for sheets of thickness 5, 10 and 20 km at different curvatures or deformation distances (the horizontal distance over which the required amplitude of sheet deformation is reached). A 300 km deformation distance is required for a 20 km thick sheet in order to have a 7 km displacement. Even for a 5 km thick sheet, which is assumed to be the thinnest subducted crust, a deformation distance of 100 km is still required. Increasing stress on the thin sheet will further increase the flexural curvature and decrease the deformation distance, but at the same time it also increases the amplitude of the displacement which exceeds the required value of 7 km. The subducted crust under the Wellington region has been determined to be approximately 20 km in thickness (Robinson 1986). This 20 km thickness was taken as the thickness of the elastic sheet. Fig. 20,**B** illustrates the deformation of this sheet under different stresses. The deformation distances of the curves, for which the displacements are within the required amplitude, are all greater than 100 km. With increasing stress the required amplitude is greatly exceeded.

The plate displacement of 7-10 km occurred within 20 km is far from being matched by the flexural deformation in either a thin or a thick plate model. This large curvature of the plate which requires to turn a horizontal slab to a steep dip must induce failure of significant sections of the plate by brittle and ductile mechanisms. The displacement can only be explained by a broken structure rather than flexural deformation. Therefore, the significant depth change in the old and rigid subducted crust under Cook Strait has to be caused by a broken structure. This torn rupture is located offshore south to the southern North Island, going cross right beneath the Wellington city. The great variations of velocity structures on its two sides in both overlying and subducted plates implies that the torn structure may have been extended downwards to as deep as 40 km and may have had great contribution to the subduction process and the geological evolution in this region. However, the problems of how deep is this torn structure extended, the nature of this faulting, its implication to the seismicity in this region, its formation time as well as its relationship to the tectonic processes associated with the evolution of Cook Strait need to be further studied.

5.4 Interpretation of the high apparent velocities

In recent 10 years, high apparent Pn velocities have been observed in the southern North Island (Kayal and Smith 1984, Reyners 1991, Galea 1992). Using a set of aftershock data from the Weber earthquake (Smith 1990), recorded on an 1 km spaced network of seismographs at Wellington, Galea (1992) observed a high apparent velocity of 8.7 km/s for the upper mantle (Fig. 22). A higher apparent velocity, 9.0 km/s, was determined by Reyners (1991) under Cape Palliser,

using the first arrivals of the Waipawa earthquake, which occurred approximately 200 km northeast of Cape Palliser and was recorded by a seismic array oriented along the east coast of the North Island (Fig. 22). High velocities of 8.80-9.01 km/s in a direction from northeast to southwest were also reported in an earlier seismic work (Kayal and Smith 1984). These velocities are anomalously larger than known upper mantle P-velocities and this was difficult to interpret. Possible reasons for these high velocities were proposed in terms of a higher velocity in the upper mantle (Kayal and Smith 1984, Galea 1992) and a dipping crustal structure (Kayal and Smith 1984, Reyners 1991). However, such high Pn velocities were not reported in an earlier extensive observation of upper mantle velocities under New Zealand (Haines 1979), which involved stations spaced approximately 130 km apart.

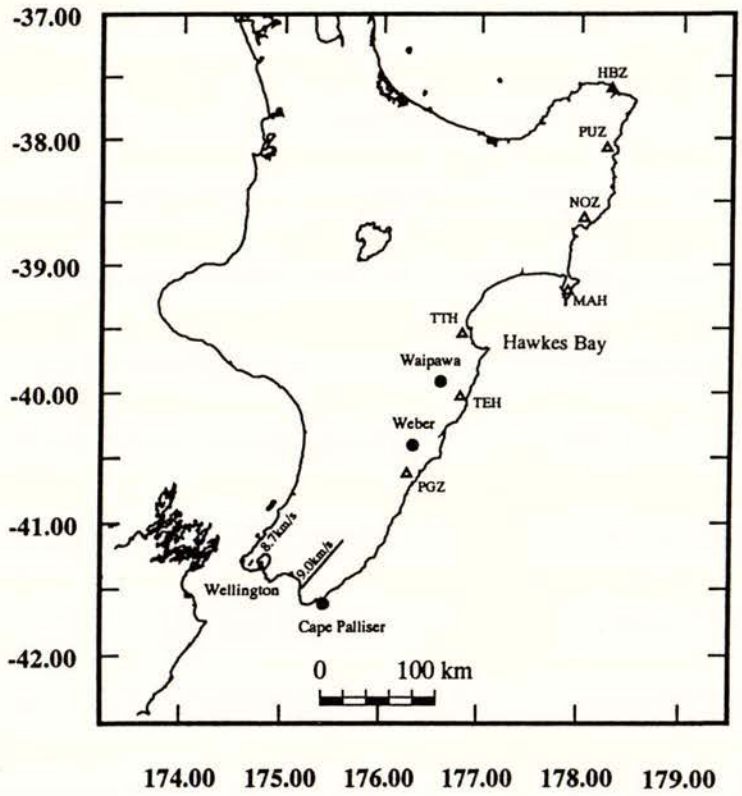

Fig. 22 Map showing apparent velocity observations. The straight solid lines near Wellington and Cape Palliser represent respectively the arrays of seismographs along which high apparent velocities, 8.7 km/s for the Weber earthquake (Galea 1992) and 9.0 km/s for the Waipawa earthquake (Reyners 1991), have been observed. The triangles represent seismic stations of the National and the Hawkes Bay Networks which recorded the main shock and the biggest aftershock of the Cape Palliser earthquakes (Luo 1992). They were used to obtain apparent Pn velocities in a reversed direction of the former observations.

A determination of high apparent velocities in the reversed direction of the former observations was performed over a distance of approximately 500 km along the east coast, using the first P-wave arrivals of the main shock and the biggest aftershock of the Cape Palliser earthquakes of 1990 (Luo 1992). Seven seismic stations spaced at approximately 60 km and approximately on the same line along the east coast with the earthquakes were used in order to comprise a natural seismic profile. Because this profile was approximately parallel to the strike of the subducted slab, the affection of the northwest subducting structure on the obtained results was neglected. Apparent velocities were determined using a linear fit method (Steinhart and Meyer 1961) to the first arrival time-epicentral distance pairs. Elevation corrections, with reference to 100m above sea level, have been applied to the arrival times using a velocity of 5.0 km/s. In all cases the corrections were less than 0.06 s in absolute value. The linear fits to the traveltime-distance pairs were made to the two data sets respectively. Both of these data sets yielded an apparent velocity of 8.55±0.15 km/s (Fig. 23). This is very similar to a velocity of 8.5 km/s obtained by Haines (1979) for the southern North Island. The failure to find high apparent velocities over an array spanning a great distance implies that the high velocities observed in the southern North Island are only locally distributed and may be caused mainly by local structures.

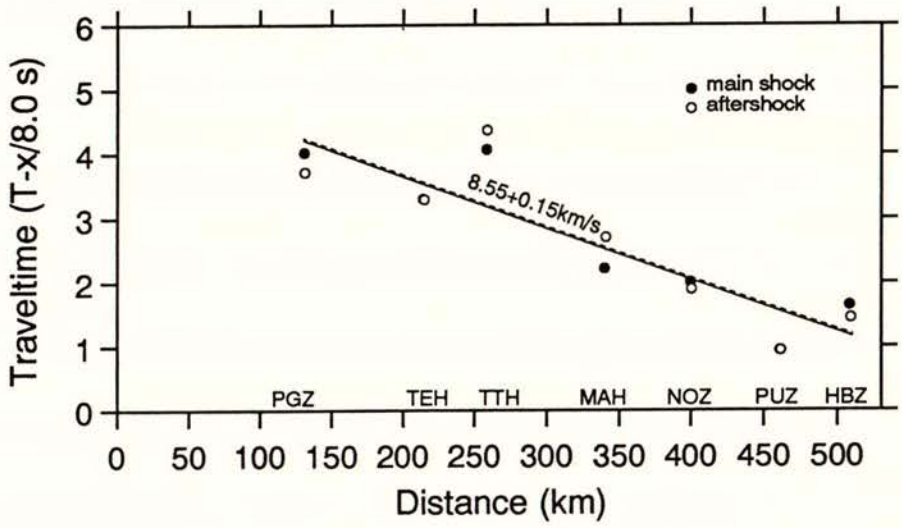

Fig. 23 P-wave travel-time (reduced) versus epicentral distance for the two Cape Palliser earthquakes. The apparent velocity was determined from linear fitting of the traveltime-epicentral distance pairs. The solid line is the fit for the main shock and the dashed line for the aftershock.

The shape of the subduction interface obtained from seismic tomographic inversion has shown that the Pacific Plate not only is subducted northwest, but also dips at approximately 3 – 4° down to the northeast under the southern North Island. On this structure, the refracted seismic rays originated from the Weber and the Waipawa earthquakes traveled actually upwards in the uppermost mantle towards the southwest before being recorded at stations arranged in the Wellington and Cape Palliser regions respectively. This updip structure is able to produce a high apparent velocity for any seismic array extending northeast at the end of the southern North Island. In order to examine the relationship between the apparent velocity amplitude and the dipping angle, a two dimensional crustal model along the strike of the subduction slab was constructed, in which a northeast dipping subducted crust was specified. This model was assumed to have four constant velocity layers as shown in Fig. 24. The thicknesses and velocities of the four layers were determined from the results obtained above and in reference to the initial velocity models used previously in seismic tomography and the velocity model obtained by Robinson (1986). The first layer was assumed to be 3 km in thickness and to have a velocity of 5.0 km/s. The second layer had a varying thickness of approximately 11-17 km and a velocity of 6.0 km/s. These two layers comprised the Australian crust. The third layer represented the subducted crust, dipping at 4° down from 13 km depth under Cape Palliser towards northeast. Beyond 90 km northeast from Cape Palliser the crust was assumed to be flat. The thickness and the average velocity for this layer were assumed to be 20 km and 7.3 km/s respectively. The bottom layer represented the upper-mantle of the Pacific plate, in which a vertical gradient velocity was assumed in order to produce efficient refraction rays. The velocity used for the top of the uppermost mantle was 8.5 km/s, in agreement with the results obtained in this study and in Haines' work (1979). At 80 km depth, 8.8 km/s was assumed. A two dimensional ray tracing method, RAY84 (Luetgert 1988) was used to find the travel-times of the rays refracted from the uppermost mantle. The Waipawa earthquake was used to generate seismic rays for a profile along the east coast near Cape Palliser. This earthquake was relocated using stations of the National Network, the Hawkes Bay Network and the seismic array with was used by Reyners (1991), and the location procedure used by Luo (1992). Receivers on the profile were assumed to be distributed within 60 km, above the dipping crust.

Significantly, ray tracing results show a high apparent velocity distribution in the Cape Palliser region (Fig. 24). The observation section of approximately 60 km northeast from Cape Palliser was divided into three segments: the beginning segment was from 35-52 km in which the seismic rays from the beginning of the dipping subducted crust were obtained; the intermediate segment was from 12-35 km; and the end segment was from -5 km to 12 km, where the rays from the most shallow dipping surface were observed. The apparent velocity determination was

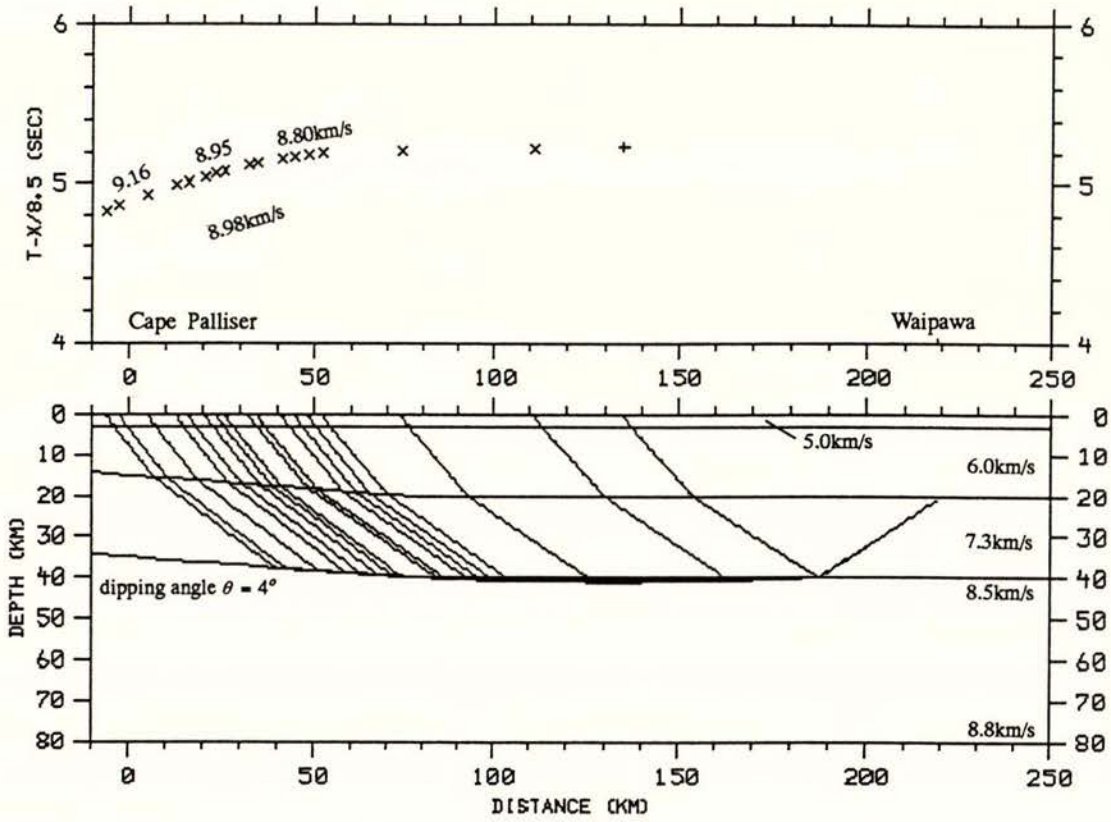

Fig. 24 Crustal structure and ray tracing diagram in a vertical cross section along the east coast. The Cape Palliser region and the location of the Waipawa earthquake are shown at the two ends of the profile. The travel-times originated from this earthquake and recorded on the ground surface near Cape Palliser are displayed using a reduction velocity of 8.5 km/s. The apparent velocities, 8.80, 8.95 and 9.16 km/s were obtained respectively over each of the three segments. An average velocity of 8.98 km/s was obtained over the three segments.

performed also using the linear fitting method. It shows a dramatical change in apparent velocity from 8.80 km/s for the beginning segment to 9.16 km/s for the end segment, increasing by approximately 4%. The average apparent velocity over the three segments was obtained to be 8.98 km/s.

The dipping angle was varied from 0 – 4. 5° in order to obtain the changes of the apparent velocities in terms of different dipping angles. Fig. 25 plots the curves of the low, high and average apparent velocities obtained on the beginning, end and over the three segments corresponding

to different dipping angles. These curves show that the apparent velocities increase nearly linearly with the increasing dipping angle. As illustrated in Fig. 25, an 8.7 km/s apparent velocity can be produced by a 1.5° dipping angle. The high apparent velocity of 9.0 km/s is able to be observed at top of Cape Palliser when the dipping angle exceeds 3°. Therefore, the high apparent velocities which have been observed in the Cape Palliser region (Kayal and Smith 1984, Reyners 1991) are most probably produced by the 3 – 4° northeast dipping subducted crust. The velocity of 8.7 km/s observed under Wellington by Galea (1992) may also be produced by this dipping structure. If the subducted plate under the Wellington region also dips approximately 3° down to the north-east, a higher average apparent velocity of approximately 8.82 km/s should be observed. The smaller velocity observed by Galea (1992) may be due to irregular ray-paths which did not travel parallelly to the strike of the subducted plate. In this work, the high apparent velocities observed in the southern North Island are fully explained by the northeast dipping structure of the subducted plate. Very high true velocities appear not to be sustained in the upper mantle under the east coast. Nevertheless, the velocity 8.5 km/s, observed by Haines (1979) and in this work is still high for the uppermost mantle compared with the values observed around the world. The reason for this high velocity is still not well understood.

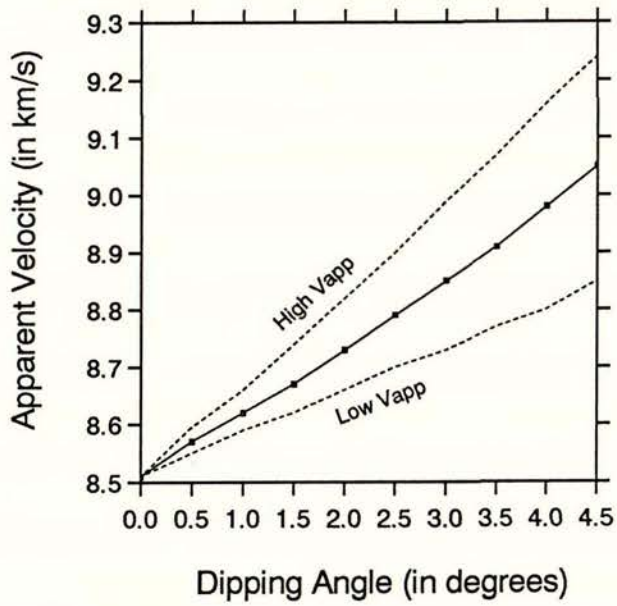

Fig. 25 Relationship between the apparent velocity and the northeast dipping angle of the subducted crust (Fig. 24). Low Vapp (the lower dashed line) represents the apparent velocity obtained for the beginning segment (see context). High Vapp (the upper dashed line) is the apparent velocity obtained for the end segment. The solid line represents the average apparent velocity for the three segments.

5.5 Morphology of the subduction interface

The morphology of the subduction interface was determined from the images of the obtained seismic velocity perturbations. The obtained result does not show that the Pacific plate has a simple northwest subduction structure under central New Zealand, but rather is broken into two pieces at the top of the southern North Island and vary in the northeast direction. This torn structure is shown to be approximately perpendicular to the strike of the subducted plate from the east to west, beneath the Wellington city. The depth of the southern plate interface is found to be consistently deeper than that of the northern interface with an offset of approximately 7-10 km. This torn structure confirms the offset of the subducted crust suggested by Robinson (1986) and perhaps correlates with the plate segmentation under Cook Strait proposed by Reyners (1983).

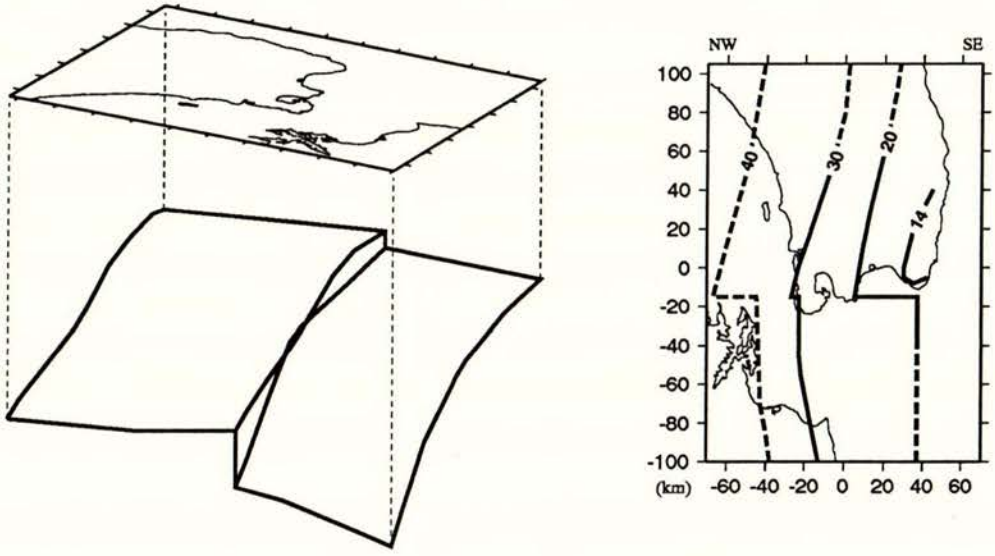

Fig. 26 Morphology of the subduction interface under central New Zealand (**A**) and depth contours of the subduction interface (**B**).

The plate interface obtained on the northern side of the torn structure not only dips northwest in the subduction direction but also dips at a 3 – 4^o angle northeast. The shallowest depth of the plate interface was determined to be approximately 13 km under Cape Palliser. This subduction configuration is supported by the high apparent velocity observations near Cape Palliser. However, high apparent velocities have also been observed along the east coast near Hawkes Bay, approximately 230 km north of Cape Palliser (Reyners 1991). It was assumed to require a southwest down dipping structure in the subducted plate under the south of Hawkes Bay in order to

produce these observed high apparent velocities (Reyners 1991). This implies that the subduction interface may have been bent or broken again somewhere between Cape Palliser and Hawkes Bay over the east coast. The shape of the subduction interface on the southern side appears to have a southwest down dipping curvature under the top of the South Island. This is in agreement with the shape of the top of the seismicity envelopes obtained south of Cook Strait (Fig. 20) and with the morphology of the subduction interface suggested by Robinson (1986) for the northern South Island. Perhaps this structure correlates with the transition of the plate subduction under the northern South Island, where the subduction of the Pacific plate becomes terminated and the continental collision occurs. South of the collision zone the Australian plate is subducted under the Pacific plate (Reyners and Cowan 1993). Fig. 26,**A** shows the morphology of the subduction interface determined from this study. The contour map of the depth of the interface is illustrated in Fig. 26,**B**.

6. CONCLUSIONS

The seismic tomographic results of this study provides the first 3-dimensional seismic image for the subduction structure under central New Zealand. The subduction interface is determined to vary in the direction parallel to the strike of the subducted plate and to be broken under northern Cook Strait. On the southern North Island, the Pacific plate not only is subducted northwest, but also dips down towards northeast at a shallow dipping angle. This northeast dipping structure is found to be the main reason for the high apparent Pn velocities which have been observed in the Cape Palliser region. The shallowest subduction interface is determined to be at the depth of approximately 13 km under Cape Palliser. From a 3-dimensional finite-difference flexural analysis on a significant change in depth of the interface, a torn structure in the subducted crust is found to be located under northern Cook Strait and to be approximately perpendicular to the strike of subduction. This torn structure is shown to be extended downwards to as deep as 40 km. It is presumed to be the largest fault trending NW-SE under central New Zealand. The subduction interface is shown to have very different shape on each side of the torn structure. On the southern side the subduction plate is found to be approximately 7-10 km deeper than that on the northern side. Under the top of the South Island the interface appears to have a southwest down-dipping curvature. Evidence from seismic images shows that the Wairau Fault extends northeast to the North Island along the east coast of the Marlborough Sounds and between the offshore of the west coast and the east of Kapiti Island towards onshore at the northwest of Otaki. An offset or bent structure of this fault is shown near the western offshore of the Wellington Peninsula where the torn structure is found. The velocity structure suggests that the northern extension of

the Wairau Fault extend downward to at least 20 km. It is presumed to be another major fault and geological boundary trending NE-SW in central New Zealand. A narrow high velocity zone is obtained above the subducted interface, along the east coast near Cape Palliser and presumed to be the reason of a horst-like subduction structure or the intrusion of fast volcanic rocks in the bottom of the overlying plate. Offshore of east Cape Palliser, a low velocity region is found. The Australian crust under Cook Strait is characterized by nearly square regions of both high and low velocity perturbations. An extensive faulting system dominated by faults in NE-SW and NW-SE trends is suggested in the Cook Strait crust.

ACKNOWLEDGEMENTS

Very special thanks to T. Webb for sending us the seismic data of the Wellington Network and the National Network for this study. Special thanks also to J. Taber, K. Gledhill, M. Chadwick and D. Francis for kindly allowing us to use the data from their temporary seismic arrays. The first author would like to thank R. Robinson, J. Taber, T. Stern, D. Walcott and M. Reyners for their valuable comments. The first author also wish to thank D. Lillis for helping the preparation of this manuscript. Thanks are also due to all colleagues of the Institute of Geophysics of VUW for the many useful discussions. We are especially grateful to The Earthquake Commission for the financial support. This research work was also partially supported by a UGC Scholarship of New Zealand, a grant from The Internal Grant Committee of VUW and a Jacob Joseph Scholarship.

REFERENCES

Adams, R. D.; Ware, D. E. 1977: Subcrustal earthquakes beneath New Zealand; locations determined with a laterally inhomogeneous velocity model. *N.Z. J. Geol. Geophys.* **20:** 59-83.

Aki, K.; Christofferson, A.; Husebye, E. S. 1977: Determination of the three-dimensional seismic structure of the lithosphere. *J. Geophys. Res.* **82:** 277-296.

Anderson, H.; Webb T., 1994: New Zealand seismicity; patterns revealed by the upgraded National Seismograph Network (in press).

Anderton, P. W. 1981: Structure and evolution of the South Wanganui Basin, New Zealand. *N. Z. J. Geol. Geophys.* **24:** 39-63.

Ansell, J. H.; Bannister, S. 1991: Morphology of the shallow subducted slab (Abstract). *Geophys. Symp., N. Z. Geophys. Soc.,* Wairakei, New Zealand.

Barnes, P. M. 1990: Provenance of Cretaceous accretionary wedge sediments: the Mangapokia Formation, Wairarapa, New Zealand. *N. Z. J. Geol. Geophys.* **33:** 125-136.

Barnes, P. M.; Korsch, R. J. 1991: Melange and related structures in Torlesse accretionary wedge,

Wairarapa, New Zealand. *N. Z. J. Geol. Geophys.* **34:** 517-532.

Bibby, H. M. 1976: Crustal strain across the Marlborough faults, New Zealand. *N. Z. Geol. geophys.,* **19:** 407-425.

Bullen, K. E. 1939: The crustal structure of the New Zealand region as inferred from studies of earthquake waves. *Proc. 6th. Pac. Sci. Congress,* 103-110.

Bullen, K. E. 1955: Note on New Zealand crustal structure. *N. Z. Trans. R. Soc.,* **82:** 995-999.

Carr, M. J.; Stoiber, R. E.; Drake, C. L. 1973: Discontinuities in the deep seismic zones under the Japanese arcs. *Bull. Geol. Soc. Am.* **84:** 2917-2930.

Carter, L.; Lewis, K. B.; Davey, F. 1988: Faults in Cook Strait and their bearing on structure of central New Zealand. *N. Z. J. Geol. Geophys.* **31:** 431-446.

Červený, V.; Klimeš, L.; Pšenčík, I. 1988: Complete ray tracing in three-dimensional structures. *in*: Doornbos, D. J. *ed*. Seismological Algorithms, Academic Press, London. Pp. 89-169.

Chase, C. G. 1978: Plate kinematics: the Americas, East Africa, and the rest of the world. *Earth Planet Sci. Lett.,* **37:** 355-368.

Clayton, R. W.; Comer, P. 1984: A tomographic analysis of mantle heterogeneities. *Terra Cognita.* **4:** 282-283.

Crosson, R. S. 1976: Crustal structure modeling of earthquake data, 1. Simultaneous least squares estimation of hypocenter and velocity structures. *J. Geophys. Res.* **81:** 3,036-3,046.

Davey, F. J.; Smith, E. G. C. 1983: A crustal seismic reflection-refraction experiment across the subducted Pacific plate under Wellington, New Zealand. *Phys. Earth Planet. Int.* **31:** 327-333.

Davey, F. J.; Hampton, M.; Childs, J.; Fisher, M. A.; Lewis, K.; Pettings, J. R. 1986: Structure of a growing accretionary prism, Hikurangi margin, New Zealand. *Geology* **14:** 663-666:

Dziewonski, A. M.; Gilbert, F. 1976: The effect of small aspherical perturbation s on travel times and a re-examination of the corrections for ellipticity. *Geophys. J. R. astr. Soc.* **44:** 7-17.

Eiby, G. A. 1968: An annotated list of New Zealand earthquakes, 1460-1965. *N. Z. J. Geol. Geophys.* **11:** 630-647.

Eiby, G. A. 1980: The Marlborough earthquakes of 1848. *N. Z. Dept. Sci. Ind. Res. Bull.,* **225,** Wellington.

Fleming, C. A.; Hutton, C. O. 1949: Notes on the geology of Kapiti Island, Cook Strait, N. Z. *N. Z. Trans. R. Soc.* **77:** 456-468.

Galea, P. 1992: Observation of very high P-velocities in the subducted slab, New Zealand, and their relation with the slab geometry. *Geophys. J. Int.* **110:** 238-250.

Garrick, R. A. 1968: A reinterpretation of the Wellington crustal refraction profile. *N. Z. J. Geol. Geophys.* **11:** 1280-1294.

George, A. D. 1988: Accretionary prism rocks of the Torlesse terrane, western Aorangi Range - Cape Palliser, New Zealand. Unpublished Ph.D. thesis, lodged in the Library, Victoria University of Wellington. 184p.

Ghani, M. A. 1974: Late Cenozoic vertical crustal movements in the central part of New Zealand. Unpublished Ph.D. Thesis, lodged in Library of Victoria University of Wellington.

Gledhill, K. R.; Randall, M. J. 1986: SNARE: an earthquake detection and recording system for

Gledhill, K. R. 1991a: EARSS users' manual, (Geophysics Division, DSIR, Wellington). *Technical Report* **97**.

Gledhill, K. R. 1991b: Evidence for shallow and pervasive seismic anisotropy in the Wellington region, New Zealand. *J. Geophys. Res.* **96:** 21503-21516.

Gledhill, K. R. 1991c: Shear-wave splitting and seismic anisotropy in the Wellington region, New Zealand. Unpublished Ph.D. thesis, lodged in the Library, Victoria University of Wellington. 237p.

Haines, A. J. 1979: Seismic wave velocities in the uppermost mantle beneath New Zealand. *N.Z. J. Geol. Geophys.* **22:** 245-257.

Hatherton, T. 1980: Shallow seismicity in New Zealand 1956-75.*N. Z. J. R. Soc.* **10:** 19-25.

Inoue, H.; Fukao, Y.; Tanabe, K.; Ogata, Y. 1990: Whole mantle P-wave travel time tomography. *Phys. Earth Planet. Int.* **59:** 294-328.

Ivory, J. M. 1986: Sheet 341, Kapiti, Gravity Anomaly Map, Coastal Series 1:250000, Wellington, New Zealand. Department of Scientific and Industrial Research of New Zealand.

Katz, H. R.; Wood, R. A. 1980: Submerged margin east of the North Island, New Zealand, and its petroleum potential. *UN ESCAP, CCOP/SOPAC Tech. Bull.* **3:** 221-235.

Kayal, J. R. 1983: A microearthquake study in a subduction zone: southeast Wellington Province, New Zealand. Unpublished Ph.D. thesis, lodged in the Library, Victoria University of Wellington. 205p.

Kayal, J. R.; Smith, E. 1984: Upper mantle P-wave velocities in the southeast North Island, New Zealand. *Tectonophysics* **104:** 115-125.

Lanczos, C. 1956: Applied Analysis. Prentice-Hall, Englewood Cliffs, New Jersey.

Lawson, C. L.; Hanson, J. H. 1974: Solving Least Squares Problems. Printice-Hall, Inc., New Jersey.

Lensen, G. J. 1958: Note on fault correlations across Cook Strait, New Zealand. *N. Z. J. Geol. Geophys.* **1:** 263-268.

Lewis, K. B.; Davey, F. J. 1987: Environment of a classical accretionary prism, Hikurangi Convergent Margin, New Zealand. *Pacific Rim Congress 87, Australia,* 263-266.

Lowry, M. A., ed. 1991: New Zealand Seismological Report 1987. Seismological Observatory Bulletin E-171, Wellington, New Zealand, Department of Scientific and Industrial Research.

Luetgert, J. H. 1988: Usr's manual for RAY84/R83PLT, interactive two-dimensional ray tracing/synthetic seismogram package. Open-file Report 88-238, United States Geological Survey.

Luo, X. 1992: Subduction interface and crustal structure in the Cape Palliser region, North Island, New Zealand, from observation of the Cape Palliser earthquakes. *N. Z. J. Geol. Geophys.* **35:** 491-499.

Luo, X. 1994: A seismic tomographic study of the subduction structure under central New Zealand. Unpublished Ph.D. thesis, lodged in the Library, Victoria University of Wellington.

McNutt, M. K.; Diament, M.; Kogan, M. G., 1988: Variations of elastic plate thickness at continental thrust belt. *J. Geophys. Res.* **93:** 8825-8838.

Moore, P. R.; Speden, I. 1979: Stratigraphy, structure, and inferred environments of deposition of the Early Cretaceous sequence, eastern Wairarapa, New Zealand. *N. Z. J. Geol. Geophys.* **22:** 417-433.

Niazi, M.; Karageorgi, E. 1992: Irregular geometry of the Gorda subduction and deep structure of the Eel River basin determined from teleseismic P delays. *Tectonophysics* **201:** 209-228.

Nolet, G. 1985: Solving and resolving inadequate and noisy tomographic system. *J. Comp. Phys.* **61:** 463-482.

Nolet, G. 1987: Seismic wave propagation and seismic tomography. *in:* Nolet G. *ed.* Seismic Tomography. D. Reidel Publishing Company, Dordrecht, Holland. Pp. 1-23.

Officer, C. B. 1959: On some offshore seismic refraction profiles in the Cook Strait, Tasman Bay, and Golden Bay areas of New Zealand. *N. Z. J. Geol. Geophys.* **2:** 350-354.

Ongley, M. 1943: Surface trace of the 1855 earthquake. *N. Z. Trans. R. Soc.* **73:** 84-89.

Paige, C. C.; Saunders, M. A. 1982a: An algorithm for sparse linear equations and sparse least squares. *ACM Trans. Math. Software* **8:** 43-71.

Paige, C. C.; Saunders, M. A. 1982b: LSQR: sparse linear equations and least squares problems. *ACM Trans. Math. Software* **8:** 195-209.

Pulliam, R. J.; Vasco, D. W.; Johnson, L. R. 1993: Tomographic inversions for Mantle *P* wave velocity structure based on the minimization of l^2 and l^1 norm of International Seismological Centre travel time residuals. *J. Geophys. Res.* **98:** 699-734.

Ramón Cabré, S. J. 1983: Geophysical studies in Central Andes. in Ramón Cabré, S. J. (ed) Geodynamics of the Eastern Pacific Region, Caribbean and Scotia Arcs, Geodynamics Series **9:** 73-76.

Reyners, M. 1980: A microearthquake study of the plate boundary, North Island, New Zealand, *Geophys. J. R. astr. Soc.* **63:** 1-22.

Reyners, M. 1983: Lateral segmentation of the subducted plate at the Hikurangi Margin, New Zealand: Seismological evidence. *Tectonophysics* **96:** 203-223.

Reyners, M. 1989: New Zealand seismicity 1964-87: an interpretation. *N. Z. J. Geol. Geophys.* **32:** 307-315.

Reyners, M. 1991: First results from the Palliser Bay-Hawke Bay seismic refraction experiment. Workshop of Tectonic Studies Group, Geological Society of New Zealand, 42-43 (abstract).

Robinson, R. 1983: Velocity structure of the Wellington region, New Zealand, from local earthquake data and its implications for subduction tectonics. *Geophys. J. R. astr. Soc.* **75:** 335-359.

Robinson, R. 1986: Seismicity, structure and tectonics of the Wellington region, New Zealand. *Geophys. J. R. astr. Soc.* **87:** 379-409.

Roecker, S. W. 1982: The velocity structure of the Pamir-Hindu Kush region: possible evidence of subducted crust. *J. Geophys. Res.* **87:** 945-959.

Rowan, L. R.; Clayton, R. W. 1993: The three-dimensional structure of Kilauea Volcano, Hawaii, from travel time tomography. *J. Geophys. Res.* **98:** 4355-4375.

Smith, E. C. C. 1990: The 1990 Weber, Southern Hawkes Bay, earthquakes: implications for the seismic hazard in Hawkes Bay. *N. Z. Geophys. Soc. Newsletter* **27:** 20-28.

Spakman, W.; Nolet, G. 1988: Imaging algorithms, accuracy and resolution in delay time tomography. In: Vlaar, N.J.; Nolet, G.; Wortel, M. T. R.; Cloetingh, S. A. P. L. (eds): *Mathematical Geophysics.* 155-187. D. Reidel Publishing Company. Dordrecht, Holland.

Spence, W. 1977: The Aleutian arc: tectonic blocks, episodic subduction, strain diffusion, and magma generation. *J. Geophys. Res.* **82:** 213-230.

Steinhart, J. S., Meyer, R. P. 1961: Minimum statistical uncertainty of the seismic refraction profile. *Geophysics* **26:** 574-587.

Stern, T. A.; Quinlan, G. M.; Holt, W. E. 1992a: Crustal dynamics associated with the formation of Wanganui Basin, New Zealand. *Sedimentary Basins of the World,* P. F. Ballance (ed.), 213-223.

Stern, T. A.; Quinlan, G. M.; Holt, W. E. 1992b: Basin formation behind an active subduction zone: three-dimensional flexural modeling of Wanganui Basin, New Zealand. *Basin Research* **4:** 197-214.

Stevens, G. R. 1974: Rugged Landscape: The geology of central New Zealand. *A. H. & A. W. Reed,* Wellington, 286p.

Suggate, R. P. 1963: The Alpine Fault. *Trans. R. Soc. N. Z.* **2:** 105-129.

Suggate, R. P.; Grindley, G. W. 1972: Geological Map of New Zealand 1:1,000,000. New Zealand Geological Survey, Wellington.

Suggate, R. P.; Stevens, G. R.; Punga, M. T. *ed.* 1978: The geology of New Zealand. Wellington, Government Printer. 2 vol. 820p.

Taber, J. J.; Smith, E. G. C. 1992: Frequency dependent amplification of weak ground motions in Porirua and Lower Hutt, New Zealand. *Bull. N. Z. Nat. Soc. Earthqk. Engineer.* **25, No. 4:** 303-327.

Taber, J.; Richardson, W. P. 1992: Frequency dependent amplification of weak ground motions in Wellington City and the Kapiti Coast. *Report to Wellington Regional Council.*

van der Sluis, A.; van der Vorst, H. A. 1987: Numerical solution of large sparse linear algebraic systems arising from tomographic problems. In: Nolet G. (ed): *Seismic Tomography.* 53-87. D. Reidel Publishing Company. Dordrecht, Holland.

Vasco, D. W. 1991: Bounding seismic velocity using a tomographic method. *Geophysics.* **56:** 472-482.

Walcott, R. I. 1970: Flexural rigidity, thickness, and viscosity of the lithosphere. *J. Geophys. Res.* **75:** 3941-3959.

Walcott, R. I. 1978a: Present tectonics and late Cenozoic evolution of New Zealand, *Geophys. J. R. astr. Soc.* **52:** 137-164.

Walcott, R. I. 1978b: Geodetic strains and large earthquakes in the axial tectonic belt of North Island, New Zealand, *J. geophys. Res.* **83:** 4419-4429.

Wellman, H. W. 1956: Structure outline of New Zealand. *N. Z. Dep. Sci. Ind. Res. Bull.* **121.**

Zhao, D.; Hasegawa, A. 1993: P wave tomographic imaging of the crust and upper mantle beneath the Japan Island. *J. Geophys. Res.* **98:** 4333-4353.